A SPACE-TIME ADAPTIVITY SCHEME FOR THE CAHN-HILLIARD EQUATION

Gabriel Freguglia Barros

Dissertação de Mestrado apresentada ao Programa de Pós-graduação em Engenharia Civil, COPPE, da Universidade Federal do Rio de Janeiro, como parte dos requisitos necessários à obtenção do título de Mestre em Engenharia Civil.

Orientadores: Alvaro Luiz Gayoso de Azeredo Coutinho
Adriano Maurício de Almeida Côrtes

Rio de Janeiro
Fevereiro de 2019

A SPACE-TIME ADAPTIVITY SCHEME FOR THE CAHN-HILLIARD EQUATION

Gabriel Freguglia Barros

DISSERTAÇÃO SUBMETIDA AO CORPO DOCENTE DO INSTITUTO ALBERTO LUIZ COIMBRA DE PÓS-GRADUAÇÃO E PESQUISA DE ENGENHARIA (COPPE) DA UNIVERSIDADE FEDERAL DO RIO DE JANEIRO COMO PARTE DOS REQUISITOS NECESSÁRIOS PARA A OBTENÇÃO DO GRAU DE MESTRE EM CIÊNCIAS EM ENGENHARIA CIVIL.

Examinada por:

Prof. Alvaro Luiz Gayoso de Azeredo Coutinho, D.Sc.

Prof. Adriano Maurício de Almeida Côrtes, D.Sc.

Prof. Fernando Pereira Duda, D.Sc.

Prof. Renato Nascimento Elias, D.Sc.

RIO DE JANEIRO, RJ – BRASIL
FEVEREIRO DE 2019

Barros, Gabriel Freguglia

A space-time adaptivity scheme for the Cahn-Hilliard equation/Gabriel Freguglia Barros. – Rio de Janeiro: UFRJ/COPPE, 2019.

XIII, 76 p.: il.; 29, 7cm.

Orientadores: Alvaro Luiz Gayoso de Azeredo Coutinho
Adriano Maurício de Almeida Côrtes

Dissertação (mestrado) – UFRJ/COPPE/Programa de Engenharia Civil, 2019.

Referências Bibliográficas: p. 64 – 71.

1. Phase-field modelling. 2. Cahn-Hilliard equation. 3. Space-time adaptivity. I. Coutinho, Alvaro Luiz Gayoso de Azeredo *et al.* II. Universidade Federal do Rio de Janeiro, COPPE, Programa de Engenharia Civil. III. Título.

À minha família.

Agradecimentos

A escrita desta dissertação de mestrado apresenta um somatório de participações, de forma direta ou indireta, de diversas pessoas em sua composição. Gostaria de agradecer, em especial:

- Inicialmente, a Deus. Sem Ele, nada disso seria possível.
- Aos meus pais, Rogério e Rosangela, e à minha irmã, Nathália, pelo apoio incondicional e pela paciência nos dias tempestuosos.
- Ao meu professor e orientador, Alvaro L. G. A. Coutinho, pela confiança, apoio, experiência, paciência e pelo seu espírito de liderança que é capaz de trazer motivação até nos momentos em que os códigos insistem em não funcionar.
- Ao meu co-orientador, Adriano M. A. Côrtes, pela paciência e empolgação em compartilhar seu vasto conhecimento em modelos de campo de fase e matemática avançada.
- Ao meu amigo de mestrado, de laboratório e de vida, Rômulo Montalvão Silva, que tantas vezes foi fundamental para dividir experiências, oportunidades e conhecimento.
- Aos meus amigos, colegas e mestres de Juiz de Fora, que desde sempre acompanharam a minha trajeória de perto, compartilharam das minhas alegrias e esticaram a mão quando mais precisei. Nesse grupo, destaco a presença constante de pessoas como Nana David, Milene Gutierrez, Cinira Vasconcelos, Lucas Novais, Matheus Cerqueira, Philippe Freguglia, Lucas Siqueira, Davi Trombini, Yuri Gondar e demais picolinos. Igualmente importantes, porém de outras cidades, gostaria de mencionar Daniel Ferreira, Rafael Vales, Diogo Aduati, Fernando Dotto, Jorge Alberto e Emerson Mourão.
- Por fim, mas não menos importante, agradeço à participação como um todo da COPPE/UFRJ e das instituições de fomento à pesquisa que tornaram possível a realização deste trabalho.

Resumo da Dissertação apresentada à COPPE/UFRJ como parte dos requisitos necessários para a obtenção do grau de Mestre em Ciências (M.Sc.)

UM ESQUEMA DE ADAPTATIVIDADE TEMPORAL-ESPACIAL PARA A EQUAÇÃO DE CAHN-HILLIARD

Gabriel Freguglia Barros

Fevereiro/2019

Orientadores: Alvaro Luiz Gayoso de Azeredo Coutinho
Adriano Maurício de Almeida Côrtes

Programa: Engenharia Civil

No presente trabalho, um esquema de adaptatividade espacial e temporal para a equação de Cahn-Hilliard é proposto. Dois indicadores de erro são testados e acoplados ao método da bissecção para a adaptatividade espacial, enquanto a adaptatividade temporal é desenvolvida sob a teoria do controle. Consideramos um estimador de erro temporal que extrapola a solução obtida por um método de integração temporal energeticamente estável e três controladores de passo de tempo: um controlador integral simples, um controlador proporcional-integrativo-derivativo completo e um controlador preditivo conhecido como PC11. Avaliamos a performance dos esquemas adaptativos para diferentes contextos físicos, como o acoplamento Navier-Stokes-Cahn-Hilliard e a equação de Cahn-Hilliard não-local, simulando diferentes físicas e escalas temporais. Valida-se a nossa estratégia com simulações bem conhecidas na literatura e avalia-se a performance para cada caso.

Abstract of Dissertation presented to COPPE/UFRJ as a partial fulfillment of the requirements for the degree of Master of Science (M.Sc.)

A SPACE-TIME ADAPTIVITY SCHEME FOR THE CAHN-HILLIARD EQUATION

Gabriel Freguglia Barros

February/2019

Advisors: Alvaro Luiz Gayoso de Azeredo Coutinho
Adriano Maurício de Almeida Côrtes

Department: Civil Engineering

In this study, we propose a space-time adaptivity scheme for the Cahn-Hilliard equation. We evaluate two error indicators for the spatial adaptivity scheme coupled with the bissection method for refinement, while the temporal adaptivity scheme is recast under the linear feedback control theory. We consider an error estimation in time that extrapolates the solution obtained from an energy-stable time marching scheme, and three time step controllers: a simple integral controller, a complete Proportional-Integral-Derivative controller, and the predictive controller known as PC11. We assess the performance of the adaptive schemes for different physical contexts for the Cahn-Hilliard equation, such as the Navier-Stokes-Cahn-Hilliard coupling and the nonlocal Cahn-Hilliard equation, simulating different physics and time scales. We validate our strategy with benchmark simulations in the literature and evaluate the performance gain for each case.

Contents

List of Figures

List of Tables

Chapter 1

Introduction

A free boundary problem (FBP) corresponds to a problem in which the domains are *a priori* unknown and have to be determined as a part of the problem solution, thanks to a number of free boundary conditions that are derived from certain physical laws or other constraints governing the phase transition, according to FRIEDMAN [8]. Probably the first classical FBP to be studied was the Stefan problem that describes the joint evolution of a liquid and a solid phase, first questioned in the nineteenth century. In the past decades, new directions were developed and new physical applications concerning free surface flows, porous media, fluid-structure interaction and crack propagation became of central importance in the FBP context (CHEN et al. [9]).

The numerical treatment of a FBP can be of great complexity. Important developments can be highlighted as:

- diffuse interface models with applications to curvature flows, solidification and phase transformations in material science;
- level set methods for evolving fronts including applications to fluid flow and image processing;
- variational front tracking methods for geometric partial differential equations (PDEs); for instance, interfaces involving curvature effects (such as surface tension and bending);
- extensive mathematical contributions to the stability, well-posedness and rigorous error analysis of discrete approximations to FBPs and degenerate nonlinear elliptic and parabolic equations; and
- adaptive methods appropriate for free boundary and interface problems.

In this study, we focus on the phase field models - more specifically, on the Cahn-Hilliard equation - which reside in the first item of the list. The phase-field models consist on the approximation of sharp interface models into thermodynamically consistent diffuse

interface models and may be understood as a mathematical theory to reformulate FBPs as PDEs that hold on a known and fixed computational domain. This strategy avoids the necessity of tracking the interfaces significantly simplifying the numerical solution of FBPs. However, the computational treatment of phase-field equations is not trivial, being an active topic of research in the computational mechanics community (GOMEZ and VAN DER ZEE [10]).

1.1 Phase-field models versus sharp-interface descriptions

In comparison with sharp-interface descriptions, phase-field models present several advantages and drawbacks. Initially, modeling free boundary problems by using sharp interface models is limited to the existence of an appropriate description of the problem to be solved, which is often not known for many classes of physical phenomena. As an example, the sharp interface model for phase separation or particle coarsening is unknown for the case when mobile dislocations and their effect of domain coarsening is included (HAATAJA et al. [11], PROVATAS and ELDER [2]). In this sense, the use of phase-field modelling yields the versatility needed to solve a practical problem of this nature since these models do not need to have a free-boundary problem associated (GÓMEZ and VAN DER ZEE [10]). They can be derived directly from free-energy functionals using the classical theory of thermomechanics and Coleman–Noll-type approaches, where constitutive equations are allowed to depend on the variational derivative of the free-energy itself (COLEMAN and NOLL [12]). Another important advantage of the phase-field models over sharp-interface descriptions is the difference of complexity during numerical simulations for both cases. Also according to PROVATAS and ELDER [2], the most challenging aspect for modelling sharp-interface descriptions is the complex interactions between topologically complex interfaces that undergo merging and pinch-off during the course of a phase transformation. These complex interactions are naturally developed in the phase-field context since the grand functional that dictates the nature of the model leads to a thermodynamically consistent interface motion without the necessity of employing any numerical procedure to validate the system.

However, since the phase-field technique lies in the concept of diffuse interface, some physical aspects may be lost in this approximation. Interfaces in real materials tend, with few exceptions, to be at most a few atoms in width, as defined for example by the extent of the strain field of interfacial dislocations (QIN and BHADESHIA [1]). Even though it is possible to narrow the interfaces on a phase field simulation to increase the accuracy of the model, the computational cost of refined meshes and and larger simulation times can be a decisive factor.

It is important to mention that, when comparing both scenarios, it is possible to reach sharp-interface models for given natural phenomena from phase-field models and vice-versa. The mathematical technique to prove the convergence of the phase-field model to the sharp-interface equation is the theory of matched asymptotic expansions (CAGINALP [13]) even though in some cases, there is still no proof that the use of the matched asymptotic expansions of a given phase-field model lead to the proper sharp-interface description of the phenomena. On the other hand, the sharp-interface model can be smoothed out to a diffuse-interface model (GOMEZ and ZEE [10]). This interplay between the two descriptions reinforces that the phase-field technique can be efficient in modelling complex phenomena with reasonable accuracy, turning the phase-field models into a promissing tool in the context of the computational mechanics.

1.2 Objectives and methodology

This study aims to assess and optimize the computational performance of the numerical solution of the Cahn-Hilliard equation in different physical contexts such as phase separation with constant and degenerate mobilities and diblock copolymers self-assembly. We consider spatial and temporal adaptivity schemes to reduce the computational effort of the simulations. The spatial adaptivity procedure aims to preserve the spatial error of a given proper mesh to model the Cahn-Hilliard equation but with a reduced number of degrees of freedom, consequently decreasing the size of the nonlinear system. The temporal adaptivity procedure aims to include the Cahn-Hilliard equation in the linear feedback control theory context, with proper error estimation and time step controller. In this study, we use three different time-step controllers with different properties and behaviors, together with a proper error estimation method that prevents the calculation of the same time step multiple times. This strategy is then coupled to a spatial adaptivity scheme to achieve maximum performance in the simulation of the Cahn-Hilliard equation. The adaptive results are compared with fixed mesh and fixed time-step simulations to show that the accuracy of the adaptive solutions is not compromised by the performance gain. The FEniCS[1] framework is a finite element library in Python/C++ and is used to solve numerically our models. The choice is due to its usability: programming a FEniCS code becomes a simple task since variational forms can be input in a near-mathematical notation. In this study we considered the stable version 2017.2.0. To post-process the results, the software Paraview[2] and MATLAB codes are used.

[1] `https://fenicsproject.org/`
[2] `https://www.paraview.org/`

1.3 Motivation

The Cahn-Hilliard equation is immersed in several different physical contexts such as diblock copolymers, image impainting, binary fluid flow, fracture propagation, tumour growth and topology optimization, according to KIM et al. [14]. The large spectrum of applications of the Cahn-Hilliard equation is responsible for its pervasive presence in computational mechanics. However, a proper numerical implementation of the phase field methods in general is a complex process, since these equations often present various temporal and spatial scales. In this sense, our motivation is to present strategies to reduce the computational effort needed to simulate the Cahn-Hilliard equation in different physical contexts while preserving the accuracy of the models.

1.4 Dissertation organization

This thesis presents the following structure: Chapter 2 describes the general physics and mathematics behind the Ginzburg-Landau functional, describing important concepts such as order parameter, interface thickness and free energy density functions. Also a Cahn-Hilliard equation approach is made, showing its derivation from the previous described functional and proving important mathematical aspects that imply on physical properties. Chapter 3 describes the computational implementation of the Cahn-Hilliard equation and all of its procedures: from the spatial finite element approximation and time integration method to the solvers used in the equations. A brief description of the computational platform FEniCS is made and some initial simulations are presented. Chapter 4 presents discussions and computational implementation on the coupling of phase-field models with fluid dynamics equations. On chapter 5, computational strategies of spatial and time adaptivity based on consistent mathematical principles are presented to reduce the computational cost of the pure Cahn-Hilliard simulations done in the previous chapter without compromising the accuracy of the model. Chapter 6 presents the evaluation of the space-time adaptivity on different physical applications for the Cahn-Hilliard equation such as the use of degenerate mobility on phase separation and diblock copolymers self assembly. Lastly, chapter 7 presents conclusions and propositions for future works.

Chapter 2

Phase-field models

The phase field method has been proved to be an interesting tool in the context of free boundary problems (BIBEN [15]). Its versatility lies in the absence of the necessity of tracking the evolution of individual interfaces, as is the case with sharp interface models, simplifying the process to numerically solve the FBPs. Figure 2.1 illustrate the difference between sharp and diffuse interface models.

2.1 Free energy functional and order parameter

Before introducing the phase field equations, the concepts of order parameter and the free energy functional must be discussed, since the nature of the phase field methods rely within the framework of irreversible thermodynamics. The order parameter is a quantity that parametrizes the change of symmetry from the disordered phase to the ordered phase appearing after a given phase transformation (PROVATAS and ELDER [2]) and may or may not have macroscopic physical interpretations. In the case of the Cahn-Hilliard equation, for example, the order parameter can be described in the literature as *concentration*,

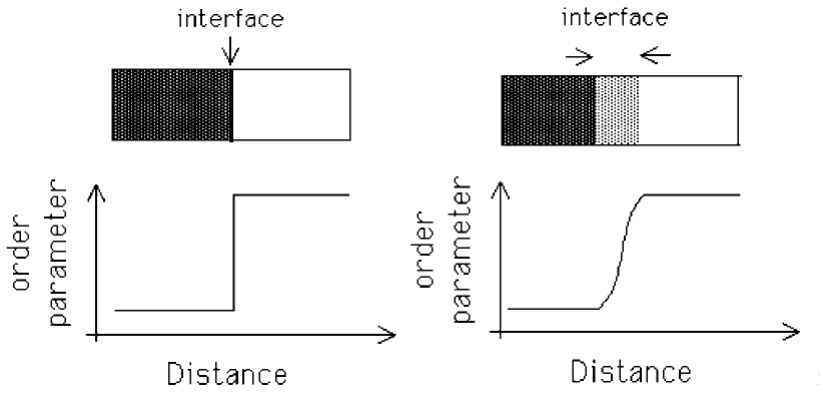

Figure 2.1: A sharp and diffuse interface model, respectively. The phase field models are diffuse interface models by definition. From QIN and BADESHIA [1]

even though it is not described by concentration physical units. The essence of the phase-field modelling is that phases and their interfaces are all represented by an order parameter - or the so-called phase field - and incorporated into a grand functional for the free energy of a heterogeneous system (QIN and BASHESHIA [1]). The interfaces are easily inferred since they become a region over which the order parameter varies between the values specified for the phases on either side.

Different free energy functionals dictates problems with different physical nature. The free energy of the system and the physics of the phase transition give rise to different phase field equations, according to PROVATAS and ELDER [2]. In this work, we focus on the Cahn-Hilliard equation and its modifications. On CAHN and HILLIARD [16], the authors proved that the free energy of a small element of a solution having a spatial variation in composition can be represented by the sum of two terms: the free energy density function or function of state, described here as $\Psi(\phi)$, being the free energy that the particle would have if surrounded by material of the same composition as itself (homogenenous mixture), and the other, named by the authors as *gradient energy* term, which is proportional to the square of the composition gradient as a first approximation. In other words, the free energy of an infinitesimal volume in a nonuniform system (or heterogeneous mixture) depends on both its composition and the composition of its nearby environment. That said, this free energy, often referred as *canonical* free energy, has the form:

$$g = \Psi(\phi) + \frac{\epsilon^2}{2}|\nabla\phi|^2, \tag{2.1}$$

where ϵ is a parameter that is constant for a regular solution and related to the interface thickness.

This functional is derived by using mixture theory and is the simplest representation of a free energy that combines the bulk thermodynamics of a simple binary alloy with a minimal description of interfacial energy. This functional, often referred as the Ginzburg-Landau functional, derives both the Allen-Cahn and Cahn-Hilliard equations (VIGNAL et al. [17]). Mathematically, the free energy functional is:

$$\begin{aligned} F[\phi] &= \int_\Omega g d\Omega \\ &= \int_\Omega \left[\Psi(\phi(\mathbf{x})) + \frac{\epsilon^2}{2}|\nabla\phi(\mathbf{x})|^2\right] d\Omega. \end{aligned} \tag{2.2}$$

The free energy density function $\Psi(\phi)$ is obtained through the Landau mean field theory in combination with statistical mechanics and thermodynamics. Proper deductions for the free energy density functions can be seen in LEE et al. [18] and PROVATAS and ELDER [2]. Figure 2.2 shows the behaviour of the free energy density function of a simple binary mixture. It is observed that, when the temperature T is less than a critical

temperature T_c, the function behaves as a double-well function of the order parameter, that is, both phases can coexist in the system. The spinodal region is defined by the spinodal lines and the mixture theory demonstrates that an initial state with $\phi = \phi_0$ quenched below these lines becomes linearly unstable to thermal fluctuations and spontaneously decomposes into the two stable phases, defined by the order parameter. The spinodal lines are found where $\partial^2\Psi/\partial\phi^2 = 0$ and are bounds to the spinodal region. LANDAU and LIFSHITZ [19] define the spinodal region as the range of concentrations where the free energy is concave and homogeneous states are unstable, giving rise to a spontaneous decomposition.

Many different free energy density functions can be derived from this statement. In this work, simulations involving pure phase-field models are entirely of isothermal spinodal decomposition, or, described by CAHN [20], a process by which a mixture of two materials can separate into distinct regions with different material concentrations. In this case, the problem is described as a second order phase transition with a symmetric phase diagram. The free energy density function in this case is a symmetric double-well function and its derivation leads to a logarithmic function. COPETTI and ELLIOT [21] proved the existence and uniqueness of the numerical solution for this case and its convergence to the solution. However, most studies in the literature approximate the logarithmic profile to a fourth order polynomial, due to its numerical advantages without compromising the phase transition (LEE [18]). It is, however, needed to be a double-well function, to make sure that both phases are coexistent. A general form is:

$$\Psi(\phi) = \frac{\alpha}{4}\left(\phi - \sqrt{\frac{\beta}{\alpha}}\right)^2\left(\phi + \sqrt{\frac{\beta}{\alpha}}\right)^2, \tag{2.3}$$

where α and β are positive constants and $\pm\sqrt{\beta/\alpha}$ define the values of $\phi_\pm$ related to the two stable bulk phases. Figure 2.3 shows its profile.

The second term of the free energy functional is relative to the *gradient energy*, according to CAHN and HILLIARD [16]. The idea behind this term is that the total free energy of the system cannot depend only on the local composition, because different spatial configurations with the same volume fraction for nonuniform systems are not energetically equivalent (BINER [22]).

Statistical mechanics define that the thermodynamical equilibrium is characterized by a state that minimizes some thermodynamic potential. To minimize the functional defined in Eq. 2.2, the global equilibrium is reached when the field variable $\phi(\mathbf{x})$ is such that:

$$\frac{\delta F[\phi]}{\delta\phi} = 0, \tag{2.4}$$

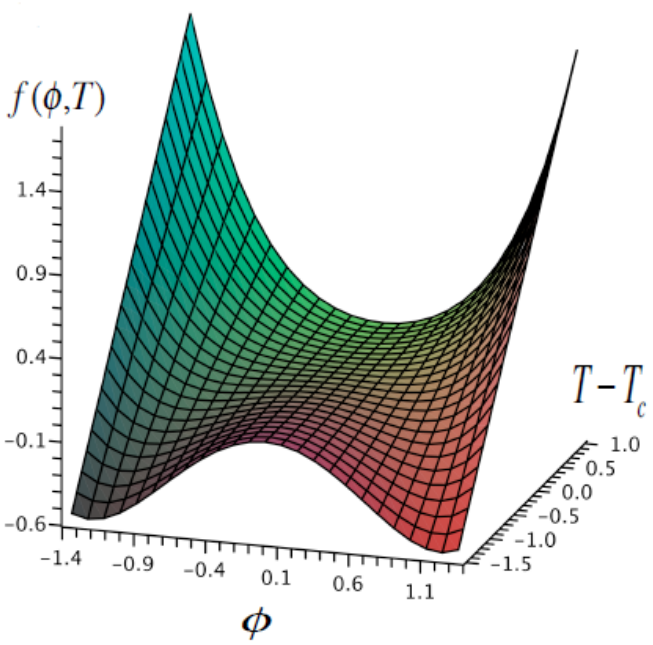

(a)

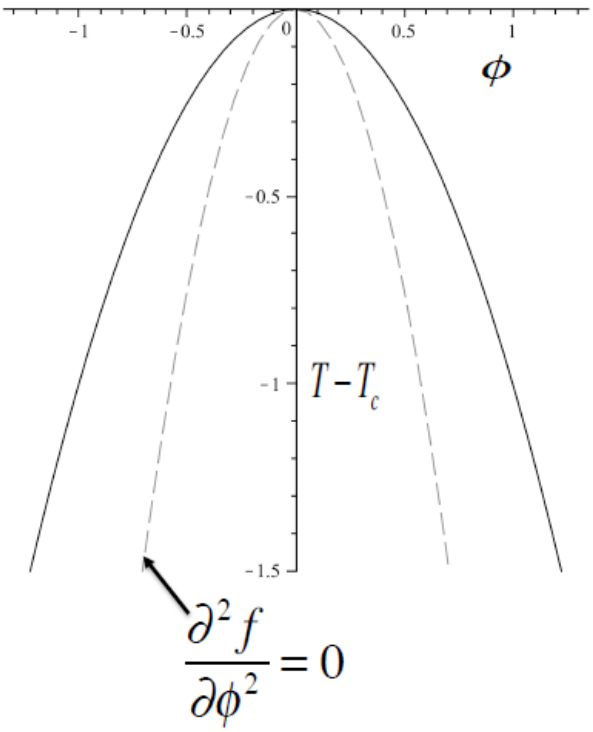

(b)

Figure 2.2: a) Energy landscape of the free energy density function of a simple binary mixture. Two stable phases arise simultaneously from one for $T < T_c$ and one single stable phase exist for temperatures above the critical temperature T_c. b) Corresponding two-phase co-existence phase diagram for $T < T_c$. The spinodal line is indicated by the gray dashed line. From PROVATAS and ELDER [2].

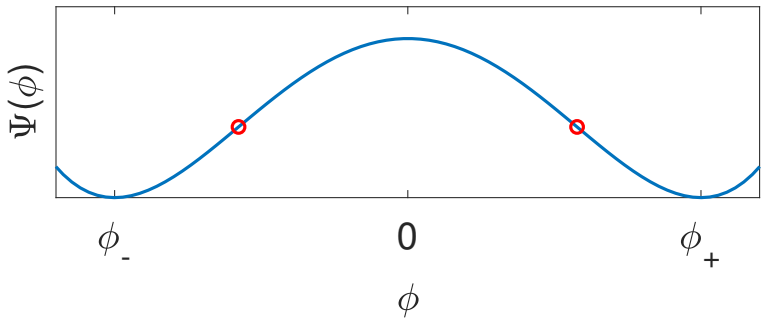

Figure 2.3: A generic free energy density function. The values of the constants α and β define the pits ϕ_- and ϕ_+ of the double-well function. The red circles are the inflection points that bound the spinodal region.

where the Gâteaux derivative operator $\frac{\delta}{\delta\phi}$ can be set as:

$$\frac{\delta F[\phi]}{\delta\phi} = \frac{\partial F[\phi]}{\partial\phi} - \nabla \cdot \frac{\partial F[\phi]}{\partial \nabla\phi}, \tag{2.5}$$

since the Ginzburg-Landau free energy functional has terms up to the first spatial derivative. The variational derivative of the free energy functional can be also translated into the chemical potential of the mixture, defined in this study as μ.

Given a generic free energy density function such as the one on Eq. 2.3, the equilibrium, according to BADALASSI *et al.* [23], becomes:

$$\begin{aligned} \frac{\delta F[\phi]}{\delta\phi} &= \mu = 0 \\ \alpha\phi^3 - \beta\phi - \lambda\Delta\phi &= 0, \end{aligned} \tag{2.6}$$

where $\lambda = \epsilon^2$.

The non-uniform one-dimensional (along a given z axis, orthogonal to the interface) solution proposed by Van der Waals which minimizes the functional is:

$$\phi_0 = \sqrt{\frac{\beta}{\alpha}}\tanh\left(\frac{z}{\sqrt{2}\xi}\right), \tag{2.7}$$

where $\xi = \sqrt{\lambda/\beta}$ is a measure of the thickness of the diffuse interface at the equilibrium. This equilibrium profile was initially proposed by VAN DER WAALS [24] for the theory of capillarity and it satisfies the boundary conditions $\phi_0(z \to \pm\infty) = \pm\phi$, according to BRAY [25]. The influence of the parameters over the thickness of the interface can be seen in Fig. 2.4.

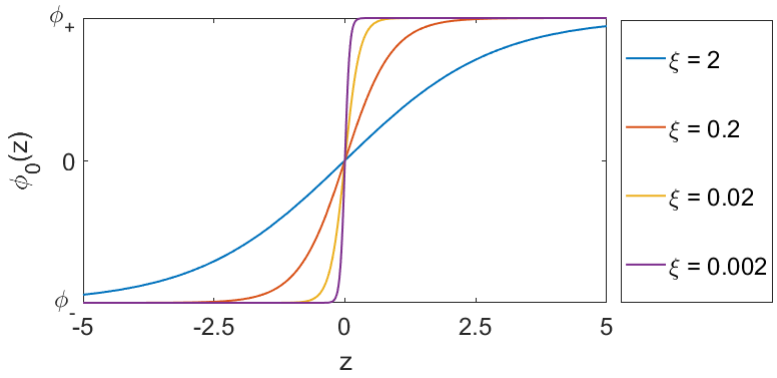

Figure 2.4: The interface width of a given profile with different parameters. We observe that for fixed α and β, high ξ values imply on a more diffuse interface.

2.2 The Cahn-Hilliard equation

The Cahn-Hilliard equation was first introduced in CAHN and HILLIARD [26] to describe the complex phase separation and coarsening phenomena in a binary alloy and has a relevant role on many physical situations and is the leading model of spinodal decomposition in binary alloys. However, many other physical applications can be seen with different setups for the Cahn-Hilliard equation. We can highlight important works such as:

- the microphase separation of diblock copolymers in OHTA and KAWASAKI [27] and CHOKSI *et al*. [28];
- impainting of binary images in BERTOZZI *et al.* [29];
- fracture propagation in BORDEN et al. [30] and SILVA et al. [31];
- tumour growth simulation in WU *et al.* [32], ODEN *et al.* and WISE *et al.* [33];
- topology optimization in ZHOU and WANG [34].

The Cahn-Hilliard equation can be seen as the H^{-1} gradient flow[1] of the free energy functional described in Eq. 2.2 that is:

$$\frac{\partial \phi}{\partial t} = \frac{\delta F[\phi]}{\delta \phi}.$$

In order to variationally derive the free energy functional, the Gateaux derivative operator, described in Eq. 2.5, must be used. Since the free energy functional depends only

[1]The H^{-1} space is the dual space of H^1, which is the Sobolev space composed by square-integrable functions whose weak first derivatives are also square-integrable functions

of the order parameter ϕ and its gradient, the variational derivative operator is as follows.

$$\frac{\delta F[\phi]}{\delta \phi} = \frac{\partial F[\phi]}{\partial \phi} - \nabla \cdot \frac{\partial F[\phi]}{\partial \nabla \phi} \tag{2.8}$$

$$= \Psi' - \lambda \nabla^2 \phi. \tag{2.9}$$

That said, considering $\bar{\Omega}$ a bounded domain, Ω as the spatial domain without the boundaries, $\partial\Omega$ its boundaries and time interval $[0, T]$, the Cahn-Hilliard equation becomes: given $\phi_0 : \Omega \to \mathbb{R}$, find $\phi : \Omega \times [0, T] \to \mathbb{R}$ such that:

$$\frac{\partial \phi}{\partial t} = -\nabla \cdot (M(\phi) \nabla (\Psi^{'} - \lambda \nabla^2 \phi)) \qquad \text{in } \Omega \times]0, T], \tag{2.10}$$

$$\phi(\mathbf{x}, 0) = \phi_0(\mathbf{x}) \qquad \text{on } \bar{\Omega}, \tag{2.11}$$

where ϕ is the order parameter that defines the phases of the mixture, $\Psi^{'}$ is the derivative of the free energy density function with respect to the order parameter variable and $\phi_0(\mathbf{x})$ is the order parameter initial conditions.

In this study, the Cahn-Hilliard equation will be used for numerically solving spinodal decomposition problems (considering the pure Cahn-Hilliard simulations), diblock copolymers self-assembly phenomena, where the Cahn-Hilliard equation inherits a nonlocal term that models the long range interactions and binary fluid flow simulations with the convective Cahn-Hilliard equation. In all situations, the most common boundary conditions are the no-flux and periodic boundaries. The no-flux boundary conditions are

$$\nabla \phi \cdot \mathbf{n} = 0 \qquad \nabla \mu \cdot \mathbf{n} = 0 \qquad \text{in } \partial\Omega, \tag{2.12}$$

being $\mathbf{n}$ the outward normal vector of the boundary $\partial\Omega$.

The use of these boundary conditions brings up two important quantities of interest: the mass conservation property and the free energy functional decay. These quantities are important to detect unphysical results in our simulations. Both proofs with proper mathematical treatment are seen on ELLIOTT and SONGMU [35]. In this study, we show how these properties are obtained without proper mathematical formalism.

Initially, the mass conservation property is shown. The null mass variation with time in the whole domain can be described as:

$$\frac{d}{dt} \int_{\Omega} \phi d\Omega = 0. \tag{2.13}$$

Integrating Eq. 2.10 all over the domain Ω and applying the divergence theorem, we

have:

$$\int_\Omega \frac{\partial \phi}{\partial t} d\Omega = \int_\Omega \nabla \cdot M(\phi) \nabla \mu d\Omega$$
$$= \int_{\partial\Omega} M(\phi) \nabla \mu \cdot \mathbf{n} d\partial\Omega. \tag{2.14}$$

Substituting the boundary conditions on Eq. 2.12 on equation 2.14, the mass conservation property is obtained considering that $\frac{\partial \phi}{\partial t} = \frac{d\phi}{dt}$:

$$\int_\Omega \frac{\partial \phi}{\partial t} d\Omega = \frac{d}{dt} \int_\Omega \phi d\Omega = 0. \tag{2.15}$$

In other words, at each time step of the simulation, the mass of the system must be exactly the same, since there is no entry or loss of matter during the process, as well as the mass of each constituent of the mixture. However, when dealing with computational simulations, these values can have a small deviation according to numerical precision, solver properties and other conditions.

Another quantity of interest of this Cahn-Hilliard setup is the free energy decrement. Fundamentally, to reach the stable situation, the total energy of the system should decrease since, thermodynamically speaking, entropy production and energy decline are the basic concepts for every physical or chemical process to take place in a closed system. Mathematically, it can be said that the energy decay of the Ginzburg-Landau functional acts as a Lyapunov function because of its monotonically decreasing behavior (VIGNAL et al [17]). Assessing the free energy decay, it can be seen, using the chain rule:

$$\frac{dF[\phi]}{dt} = \frac{\delta F[\phi]}{\delta \phi} \frac{\partial \phi}{\partial t}. \tag{2.16}$$

Substituting the variational derivative of $F[\phi]$ on Eq. 2.16, using the divergence theorem and applying the boundary conditions presented in Eq. 2.12:

$$\frac{dF[\phi]}{dt} = \int_\Omega \mu \frac{\partial \phi}{\partial t} d\Omega$$
$$= \int_\Omega \mu \nabla \cdot (M(\phi) \nabla \mu) d\Omega$$
$$= \int_{\partial\Omega} \mu M(\phi) \nabla \mu \cdot n d\partial\Omega - \int_\Omega \nabla \mu \cdot (M(\phi) \nabla \mu) d\Omega$$
$$= - \int_\Omega M(\phi) |\nabla \mu|^2 d\Omega \leq 0. \tag{2.17}$$

Since mobility $M(\phi)$ is a positive function (or constant), the energy stability relies on a Lyapunov function, that is, the free energy functional is monotonically decreasing and the chosen time integration method must possess this property (VIGNAL et al. [17]).

Chapter 3

Computational implementation of the Cahn-Hilliard equation

In this chapter we present details of the numerical implementation of the pure Cahn-Hilliard equation. The Cahn-Hilliard equation is notoriously difficult to solve numerically because the equations are stiff due to both the biharmonic operator and the nonlinear operator (EYRE [36]) aside from the fact that across the spatial interfaces, the solution undergoes an $\mathcal{O}(1)$ change over an $\mathcal{O}(\epsilon)$ interval.

In this chapter, we describe how the Cahn-Hilliard equation should be discretized and approximated by our methods of choice, in order to guarantee accuracy in our results. Special attention is required to spatially discretize the domain by using the standard C^0 finite elements and a proper time integration method.

3.1 The finite element method

In this study, we use the finite element method to spatially approximate the pure Cahn-Hilliard equation and the modified nonlocal Cahn-Hilliard equation. In this section, we describe the standard finite element method, that will be used in the simulations of the pure Cahn-Hilliard and the nonlocal Cahn-Hilliard equations in chapters 3 and 5.

Finite element approximations are based on a variational form (or weak form) of the PDE. The weak form of a PDE is obtained by multiplicating the PDE by a test function $w(\mathbf{x})$ from a proper space function and integrating all over its domain. The Galerkin method is used to approximate the solutions from a infinite dimension space to a finite one. Equation 3.1 shows this approximation, where $u(\mathbf{x})$ is the exact solution of the PDE in the weak form, $\hat{u}(\mathbf{x})$ is the approximate solution, $N_i(\mathbf{x})$ are the basis functions and $\tilde{u}_i(t)$ are the unknown variables, such that:

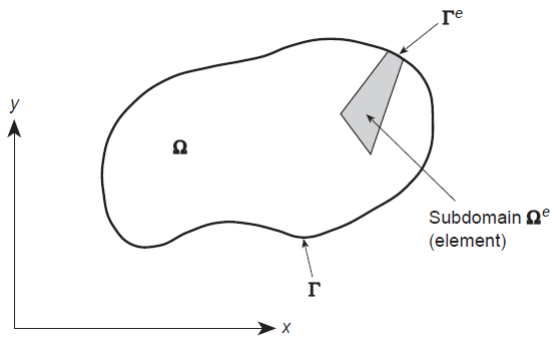

Figure 3.1: Graphical representation of a bidimensional domain divided into subdomains (elements). Adapted from ZIENKIEWICZ [3]

$$u(\mathbf{x}) \approx \hat{u}(\mathbf{x}) = \sum_{i=1}^{n} N_i(\mathbf{x})\tilde{u}_i(t), \tag{3.1}$$

$$w(\mathbf{x}) = \sum_{i=1}^{n} N_i(\mathbf{x})w_i(t). \tag{3.2}$$

The standard finite element method consists on discretizing a spatial domain $\Omega \subset \mathbb{R}^{nsd}$, with boundaries $\Gamma \subset \mathbb{R}^{nsd-1}$ into a mesh composed by nodes and elements. In this case, the unknown variables $\tilde{u}_i(t)$ are also defined as nodal values. Each element is composed by its domain $\Omega^e \subset \mathbb{R}^{nsd}$ and boundary $\Gamma^e \subset \mathbb{R}^{nsd-1}$. Figure 3.1 illustrates a finite element method domain. Mathematically speaking, the discretization of the spatial domain Ω into nel number of elements is such that:

$$\begin{cases} \Omega = \cup_{e=1}^{nel} \Omega^e, \\ \emptyset = \cap_{e=1}^{nel} \Omega^e. \end{cases} \tag{3.3}$$

The Galerkin isoparametric formulation is used to approximate the pure Cahn-Hilliard and the nonlocal Cahn-Hilliard equations in this study, so that all functions are interpolated in the domain using the same basis functions N_i. The basis function N_i are illustrated on Fig. 3.2 and must respect the compact support condition presented as:

$$N_i(x_j) = \delta_{ij}, \tag{3.4}$$

where δ_{ij} is the Kronecker delta. The compact support property added to the domain subdivision seen on equation (3.3) allows us to represent the variational formulation integrals over the complete domain as a sum of the integral inside each element. Since the integration of each element is required, a reference space ξ is used where the definition of the basis functions in the element are well defined, enabling the use of well known quadrature rules, assisting on the automation of the process.

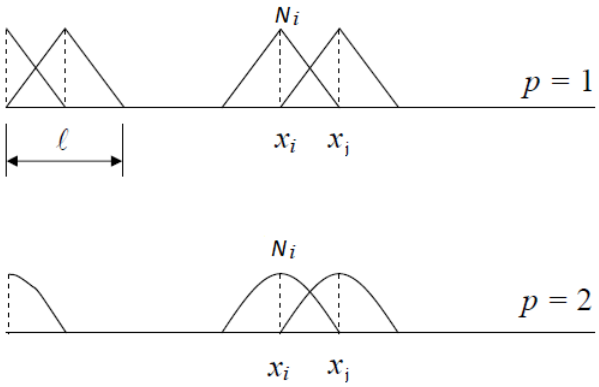

Figure 3.2: Illustration of polynomial basis functions (linear and quadractic, respectively).

In order to be spatially approximated by the finite element method, the Cahn-Hilliard equation must be expressed in its weak form. One of the main difficulties when using the finite element method on the Cahn-Hilliard equation is that, due to the presence of the biharmonic operator in its description, standard C^0-continuous finite elements are not suitable for the primal variational formulation of the Cahn-Hilliard equation. To circumvent this constraint, several studies presented different strategies: STOGNER *et al.* [37] presented a C^1-continuous finite element formulation for rectilinear grids, GÓMEZ *et al.* [38] explored the NURBS-based variational formulation, enabling the possibility of 3D simulations using the primal description, and WELLS *et al.* [39] using a discontinuous Galerkin method. In this study we consider a splitting strategy, also called mixed formulation, that avoids the continuity constraint and enable the use of C^0-continuous elements, converting the Cahn-Hilliard equation into a coupled nonlinear system, with an additional degree of freedom per node (ELLIOT *et al.* [40]). This reformulation also reduces the complexity of the problem from the numerical point of view (VAN DER ZEE *et al.* [41]). In this study, we take advantage of the splitting strategy for the Cahn-Hilliard equation and use the finite element method with a choice of linear basis functions. Recovering the identity $\mu = \dfrac{\delta F}{\delta \phi}$, we can split eq. 2.10 into:

$$\frac{\partial \phi}{\partial t} - \nabla \cdot M(\phi) \nabla \mu = 0 \qquad \text{in } \Omega, \tag{3.5}$$

$$\mu - \Psi^{'} + \lambda \nabla^2 \phi = 0 \qquad \text{in } \Omega. \tag{3.6}$$

From the splitting technique, unknown fields now become $\phi(\mathbf{x}, t)$ and $\mu(\mathbf{x}, t)$ and a test function for each equation must be used, that is, $w(\mathbf{x})$ and $q(\mathbf{x})$. The weak form of the system can be obtained by integrating both Eqs. 3.5 and 3.6 in their strong form against weighting functions $w, q \in H^1(\Omega)$, where $H^1(\Omega)$ is the Sobolev space of the square integrable functions with an integrable first weak derivative, and applying the divergence theorem. Being $P^k(\Omega^e)$ the space of polynomials of degree equal or less than k over Ω^e,

the function spaces are defined as:

$$S_t^h = \{\phi^h(\cdot,t), \mu^h(\cdot,t) \in H^1(\Omega) \mid \phi^h(\cdot,t)|_{\Omega_e}, \mu^h(\cdot,t)|_{\Omega_e} \in P^k(\Omega^e), \forall e\}, \tag{3.7}$$

$$W^h = \{w^h, q^h \in H^1(\Omega) \mid w^h|_{\Omega_e}, q^h|_{\Omega_e} \in P^k(\Omega^e), \forall e\}. \tag{3.8}$$

Therefore, the semi-discrete finite element formulation for the Cahn-Hilliard nonlinear system is: find $\phi^h(t), \mu^h(t) \in S_t^h, \forall w^h, q^h \in W^h$, so that:

$$\begin{aligned} \left(w^h, \frac{\partial \phi^h}{\partial t}\right) + (\nabla w^h, M(\phi^h)\nabla \mu^h) = 0, \\ (q^h, \mu^h) - (q^h, \Psi^{'}) - (\nabla q^h, \epsilon^2 \nabla \phi^h) = 0, \end{aligned} \tag{3.9}$$

where the $\mathcal{L}^2$ inner product over the domain Ω is indicated by $(\cdot,\cdot)_\Omega$ and:

$$\begin{aligned} w^h &= \sum_{k=1}^{n_{nodes}} c_{\phi_k} N_k, & \phi^h &= \sum_{k=1}^{n_{nodes}} \phi_k N_k, \\ q^h &= \sum_{k=1}^{n_{nodes}} c_{\mu_k} N_k, & \mu^h &= \sum_{k=1}^{n_{nodes}} \mu_k N_k, \end{aligned} \tag{3.10}$$

where N_k are the interpolation functions, n_{nodes} is the number of the nodes in the finite element mesh and c_{ϕ_k} and c_{μ_k} are arbitrary constants.

3.2 Time integration

The Cahn-Hilliard equation is a time-dependent equation, so a proper time integration method must be chosen. The choice of a proper time integration method for the Cahn-Hilliard equation is not a trivial task. As shown in section 2.2, the free energy functional is a Lyapunov functional when no-flux or periodic boundary conditions are applied to the domain. Since these boundary conditions comprehend most of the situations where the Cahn-Hilliard equation is employed, it is fundamental that the time integration method used respect the free energy decay in every possible situation. In other words, for any given time step n, the following inequality must be respected:

$$F[\phi_{n+1}] - F[\phi_n] \leq 0. \tag{3.11}$$

According to GÓMEZ and VAN DER ZEE [10], the choice of a proper time integration method for the Cahn-Hilliard equation must respect the following items:

- The order of accuracy of the scheme;
- The stability of the algorithm;

- The solvability of the time-discrete equations;

Initially, in the context of numerical analysis, the order of accuracy quantifies the rate of convergence of a numerical approximation of a differential equation to the exact solution. That is, in the time integration context, the larger the order of accuracy of the method, the faster the error diminishes with the reduction of the time step size Δt. Proceeding to the second item, the stability of an algorithm is a clear concept in the context of linear problems. However, for nonlinear problems, the concept of stability becomes much more complex and difficult to be defined. In the Cahn-Hilliard equation context, stability is often treated as the energy-stability described in Eq. 3.11. That is, time integration methods can be unconditionally energy-stable, where Eq. 3.11 is respected independently of the size of the time step Δt or conditionally energy-stable, where the time step cannot assume larger sizes than a critical Δt_c. Lastly, the concept of solvability lies in the observation that when the time step is too large, depending on the method employed the Cahn-Hilliard equation can present multiple solutions (EYRE [36]).

About the nature of a time integration scheme to be chosen, explicit methods are often prohibitive due to severe restrictions on the time step size, which is around $\mathcal{O}(\Delta x^4)$, arising from the stiffness of the equation, while fully implicit schemes require the use of nonlinear solvers. An intermediate approach is provided by semi-implicit time-stepping algorithms, where some terms are treated implicitly while others are treated explicitly. The convex-splitting scheme solves the problem of the unicity of the solution, such that the solution is the Euler-Lagrange equation of a given convex energy functional, thus being its minimizer, and is also unconditionally energy stable (EYRE [36], ELLIOT and STUART [42]). However, these properties are only guaranteed on the first order convex-splitting method. Second order convex-splitting schemes do not present a general form, depending on the structure of $\Psi(\phi)$ and require proper stabilization to be unconditionally energy-stable and uniquely solvable (SHEN [43]).

That said, VIGNAL *et al.* [17] proposed the method chosen in this study. This method is mathematically proven to be energy stable regardless of mesh and time step size and is second-order accurate in time, even though it is restricted on the use of a quartic potential, which is the case of this study. The energy stability is proven by expanding the nonlinear terms into Taylor's series. On the solvability criteria, this method suits the adaptive time stepping strategy proposed, allowing larger time steps without compromising the accuracy of the model since the proposition of the method was tested with similar adaptive time stepping strategies (VIGNAL *et al.* [17]). Applying the time integration method on the variational formulation of the problem in Eq. 3.9, considering the initial conditions $\phi(\mathbf{x}, 0) = \phi_0$ and $\mu(\mathbf{x}, 0) = \mu_0$, where μ_0 is an arbitrary function, the fully discrete system is as follows:

$$\begin{cases} \left(w^h, \dfrac{[\![\phi]\!]}{\Delta t_{n+1}}\right)_\Omega + (\nabla w^h, M_{n+1}\nabla\mu^h_{n+1})_\Omega & = 0, \\ (q^h, \mu^h_{n+1}) - (q^h, \tilde{\Psi}')_\Omega - (\nabla q^h, \epsilon^2\nabla\{\phi\})_\Omega & = 0, \end{cases} \tag{3.12}$$

where:

$$[[\phi]] = \phi^h_{n+1} - \phi^h_n, \qquad \Delta t_{n+1} = t_{n+1} - t_n, \qquad \{\phi\} = \frac{\phi^h_{n+1} + \phi^h_n}{2}.$$

The function $\tilde{\Psi}'$ represents an approximation to Ψ' such that the scheme is energy-stable. The approximation is defined as:

$$\tilde{\Psi}' = \frac{\partial\Psi_{n+1}}{\partial\phi} - \frac{\partial^2\Psi_{n+1}}{\partial\phi^2}\frac{[\![\phi]\!]}{2} + \frac{\partial^3\Psi_{n+1}}{\partial\phi^3}\frac{[\![\phi]\!]^2}{6}. \tag{3.13}$$

3.3 The nonlinear system solver

The solution of the nonlinear system seen on equation (3.12) in the present study is reached by using the Newton method. The Newton method first appeared in the 17th century and is one of the most robust methods in solving nonlinear systems (KELLEY [44]). The Newton method consists on linearizating a nonlinear system by iterating a Taylor expansion on given a function $\mathbf{R}(\phi)$ until the first order term from ϕ on a given iteration k, such that:

$$\mathbf{R}(\phi^h_{k+1}) = \mathbf{R}(\phi^h_k) + \mathbf{R}'(\phi^h_k)(\phi^h_{k+1} - \phi^h_k) + \mathcal{O}(\Delta\phi^h)^2. \tag{3.14}$$

Ignoring the second order terms and making $\mathbf{R}(\phi^h_{k+1}) = 0$, the following identity can be reached:

$$\mathbf{J}\delta\phi^h_k = -\mathbf{R}(\phi^h_k), \tag{3.15}$$

where $\delta\phi^h_k = \phi^h_{k+1} - \phi^h_k$ and $\mathbf{J} = \mathbf{R}'(\phi^h_k)$.

The nonlinear system becomes now a sequence of linear systems. Equation (3.15) is linearly solved for $\delta\phi^h_k$ and, using the relation $\phi^h_{k+1} = \phi^h_k + \delta\phi^h_k$, the iteration $k+1$ is reached. The iterator k is increased from $k = 0$ (from an initial guess) until a maximum number of iterations n_{iter} and/or the nonlinear residual reach a given absolute tolerance tol_{res} and/or the variable update is smaller than a relative tolerance tol_{update}. Both tolerance relations are:

$$\frac{||\mathbf{R}(\phi^h_k)||}{||\mathbf{R}(\phi^h_0)||} < tol_{res} \qquad \frac{||\delta(\phi^h_k)||}{||(\phi^h_k)||} < tol_{update} \tag{3.16}$$

In this study, we consider the relative tolerance as a stopping criteria with a prescribed value of 10^{-4}, that is $tol_{res} = tol_{update} = 10^{-4}$.

3.4 The linear system solver

As described in the previous section, the nonlinear system now becomes a sequence of linear systems. The system described by equation (3.15) can be seen as $\mathbf{Ax} = \mathbf{b}$. The linear systems generated in the simulations in this study are large due to fine meshes needed to accurately define the interfaces and the splitting technique, that provides an extra degree of freedom for each node, doubling the size of the unknown vector. It is well known from the numerical analysis that large linear systems are better solvable by iterative methods (KELLEY [44]). In this sense, we choose the Generalized Minimum RESidual (GMRES) linear solver, a very efficient iterative method for nonsymmetric system of linear equations and used in several papers involving phase-field modelling, such as VIGNAL et al. [17] and WODO and GANAPATHYSUBRAMANIAN [45].

The Krylov iterative methods consist on the projection of the subspace $\mathbf{K_j}$ of dimension j given on equation 3.17 where $\mathbf{r_0} = \mathbf{b} - \mathbf{Ax_0}$.

$$\mathbf{K_j} = span(\mathbf{r_0}, \mathbf{Ar_0}, ..., \mathbf{A^{j-1}r_0}). \tag{3.17}$$

Applying this method on equation 3.15 on a given iteration k, we reach:

$$\mathbf{r_0} = -\mathbf{J}\delta\phi - \mathbf{R}(\phi). \tag{3.18}$$

The GMRES method consist on minimizing $||\mathbf{J}\delta\phi + \mathbf{R}(\phi)||_2$ for each iteration of the method, where $\delta\phi$ is given on equation 3.19 and τ_i are scalars that minimize the residual:

$$\delta\phi_\mathbf{j} = \delta\phi_\mathbf{0} + \sum_{i=0}^{j-1} \tau_i (\mathbf{J})^i \mathbf{r_0}. \tag{3.19}$$

A common practice when using iterative methods is to combine them with a preconditioning method in order to speed up convergence. A robust preconditioning method that works fine with the GMRES method is the Incomplete LU factorization (ILU) method. The ILU method consist on approximating the matrix $\mathbf{A}$ into a product of two matrices: a lower triangular $\mathbf{L}$ and an upper triangular $\mathbf{U}$ matrix. This is useful in the treatment for a sparse matrix, in the sense that the LU factors can be much less sparse than the original matrix, reducing memory requirements and making the convergence faster. In this study, the linearized systems are solved by PETSc's ILU(0)-GMRES(35) with a prescribed relative tolerance of 10^{-5}.

3.5 The FEniCS framework

The Finite Elements nurtured in Computer Science (FEniCS) framework is an open-source computing platform for solving partial differential equations using the finite element method (ALNÆS et al. [4], LOGG et al. [46]). Its structure consists on several built-in functions that can be translated into simplicity to novice programmers or performance to more experienced users. FEniCS consists of a number of building blocks (software components) that together form the FEniCS software. Figure 3.3 shows its structure.

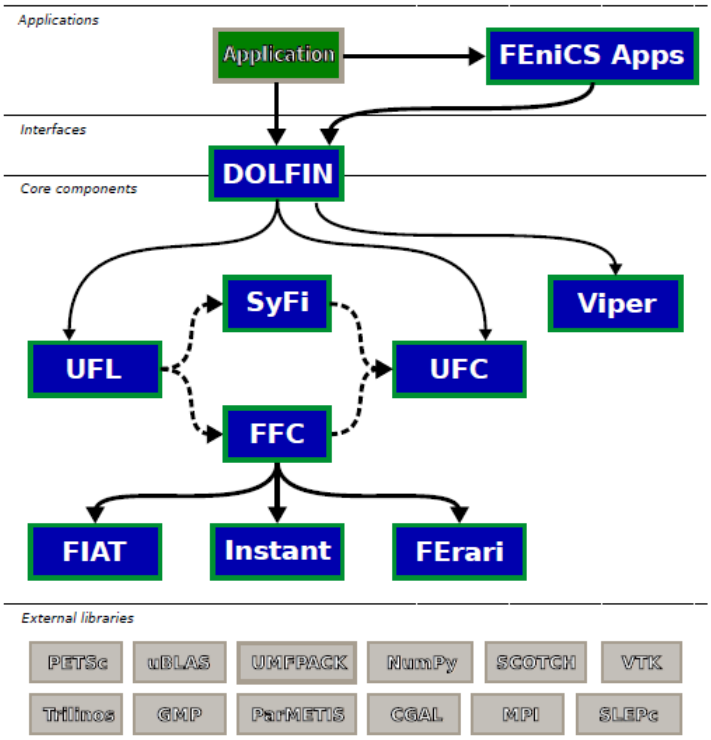

Figure 3.3: FEniCS software and its components. From LOGG et al. [4].

From the FEniCS structure, some important components can be highlighted:

- DOLFIN is a C++/Python library that functions as the main user interface of FEniCS. It provides a problem solving environment for models based on partial differential equations and implements core parts of the functionality of FEniCS, including data structures and algorithms for computational meshes and finite element assembly.

- FFC is the FEniCS form compiler. It is responsible for converting the equation's variational form in the code into matrices, tensors and vectors in a efficient and error-free way.

- UFL is the Unified Form Language, and can be seen as the core component of the

FEniCS framework. It is responsible for automating the process of the problem definition, given the variational formulation of the problem.

The reason why the FEniCS framework was selected for this study was its simplicity of implementation the variational formulation without the necessity of explicited matrices treatment, which is automated in an optimized way: the data structure is automated to integrate each element, assemble the local matrix to a global matrix and solve it with the PETSc (BALAY *et al.* [47]) or Trilinos (HEROUX *et al.* [48]) solvers. For example, our variational formulation on equation (3.12) can be written as:

```
Form0 = w*phi_form0/dtt*dx + inner(grad(w),M*grad(mu))*dx
Form1 = q*(mu-dpsitil)*dx - inner(grad(q),lmbda*grad(phi_form1))*dx
Form = Form0 + Form1
```

This simplicity makes the code writing much easier and efficient. Also, the data structure and solver implementations used are well known standard libraries.

3.6 Spinodal decomposition: initial simulations

In order to evaluate every method presented in this study, a phase-separation process simulation with the Cahn-Hilliard equation is made to verify the quantities of interest presented in chapter 2. The initial condition has the form:

$$\phi(\mathbf{x}, 0) = \bar{\phi} + r, \tag{3.20}$$

where r is a random variable with uniform distribution in $[-0.01, 0.01]$ and $\bar{\phi}$ is set to be 0.3, being inside the spinodal region described in Fig. 2.3. The simulations consist on a unit square domain $\bar{\Omega} = [0, 1] \times [0, 1]$ discretized into an uniform mesh of $[128]^2$ C^0 linear elements. The following parameters are used: $\alpha = 100$, $\beta = 100$, $\lambda = 0.01$, $M(\phi) = 1$ and $\Delta t_{n+1} = 2 \times 10^{-6} s$ for all time steps.

The initial condition is seen on Fig. 3.4 and represents an unstable mixture (GOMEZ *et al.* [38]). This instability triggers an initial spinodal decomposition, which results in two coexisting phases being formed, and is followed by coarsening in later stages, whereby the two distinct phases grow with time to decrease the total interfacial area. The simulations are described in snapshots in Fig. 3.5. Since the fixed time step needs to be small in order to capture the fast dynamics of the initial stages of the spinodal decomposition, reaching the steady-state without any time step adaptivity strategy requires thousands of time steps. In this sense, the steady state is not reached in fixed time step simulations, limiting this section to 5000 time steps. That is, the fixed time step simulation simulation ends at $t = 0.01$ s.

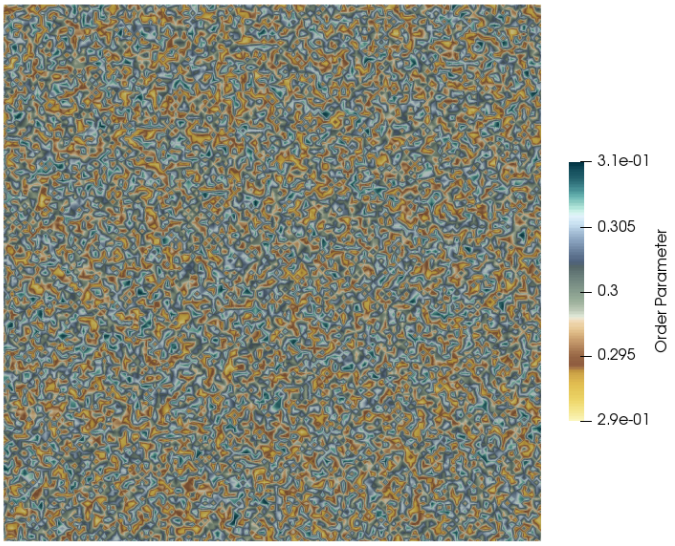

Figure 3.4: Initial condition for all the spinodal decompositions in this study.

On the early stages of the simulation, the phases begin to be segregate. The order parameter that started the simulation around 0.3 starts to approach the values defined by the free energy density function. In our simulations, for $\alpha = 100$ and $\beta = 100$, it has the form:

$$\Psi(\phi) = 25(\phi^2 - 1)^2, \tag{3.21}$$

where phases ϕ_- and ϕ_+ are defined to be as $\phi = -1$ and $\phi = 1$, respectively.

After the phase definitions, the concentrations of each component begin the different processes of interaction, such as pinch-offs and coalescences. On the late stages of the simulation, the droplets with smaller concentrations were already absorbed by the larger ones and, at this point, the solution practically does not change during the time evolution. This is the point where the time adaptivity schemes are expected to improve the efficiency of the simulation, admitting larger time steps. This is discussed in depth in section 5. Figure 3.5 confirms this behavior, describing the evolution of the phase field submitted to the spinodal decomposition of the simulations with constant mobility. We can observe that the Figs. 5.2a, 5.2b and 5.2c present rapid dynamics, revealing more significant changes in the phase field while Figs. 5.2d, 3.5e and 3.5f present slower dynamics, with more subtle changes in the phase field even though the time difference between them is much larger then the previous three figures. As mentioned before, some quantities of interest are also assessed to verify the validity of our models. The mass variation in time and energy decay are seen in Fig. 3.6. The mass variation figure describes $M(t)/M_0$, where $M(t)$ is the mass of the system during the simulation and M_0 is the mass of the system at the initial stage. The mass variation is within the range of the numerical tolerance of the solver, being around 2%. The energy decay is also seen proving that during all the simulation the energy levels kept decreasing.

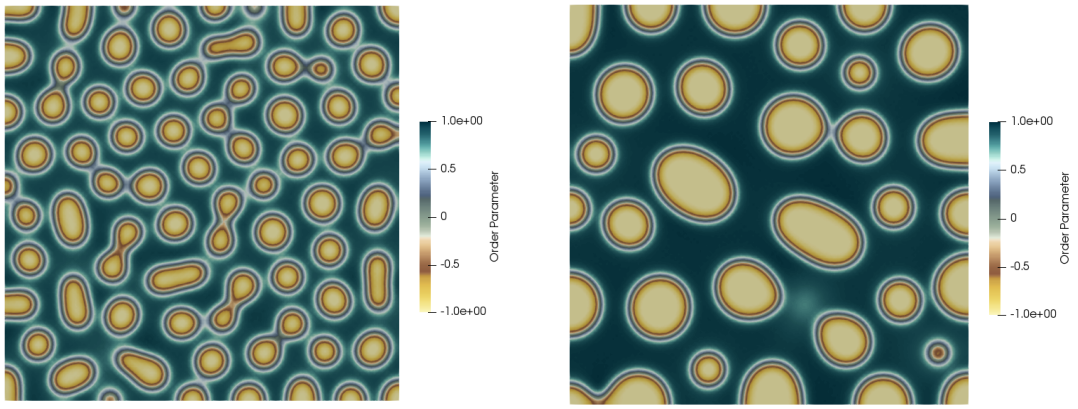

(a) $t = 0.0001s$ (b) $t = 0.0005s$

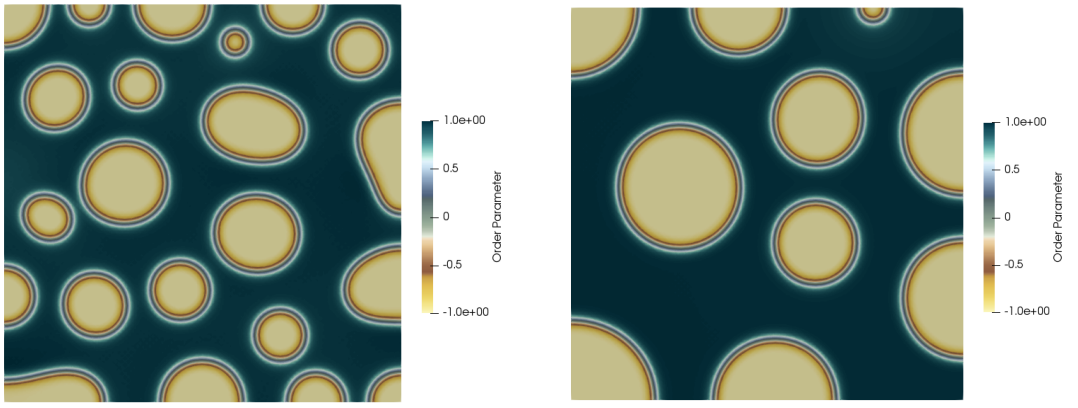

(c) $t = 0.0010s$ (d) $t = 0.0050s$

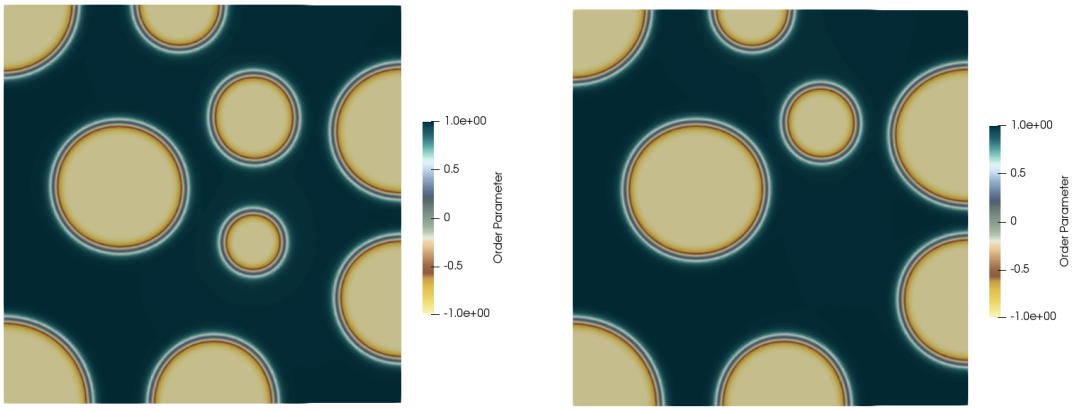

(e) $t = 0.0075s$ (f) $t = 0.0100s$

Figure 3.5: Spinodal decomposition using fixed time step and fixed mesh at different times.

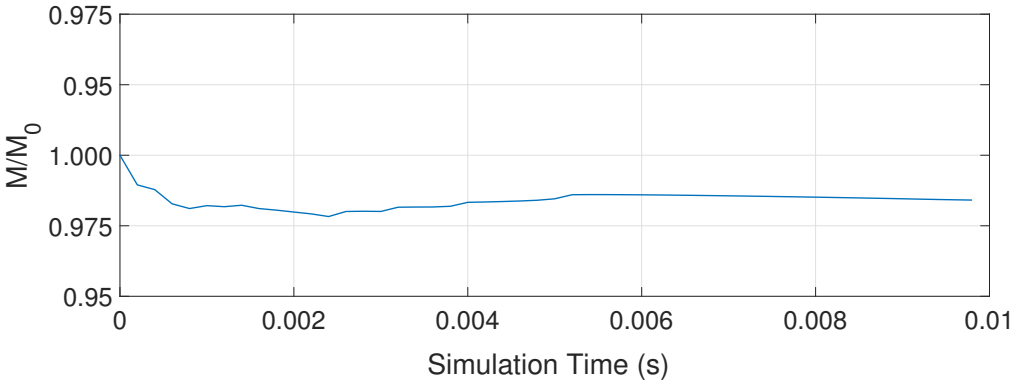

(a) Mass variation compared to the initial conditions. $M(t)/M_0$.

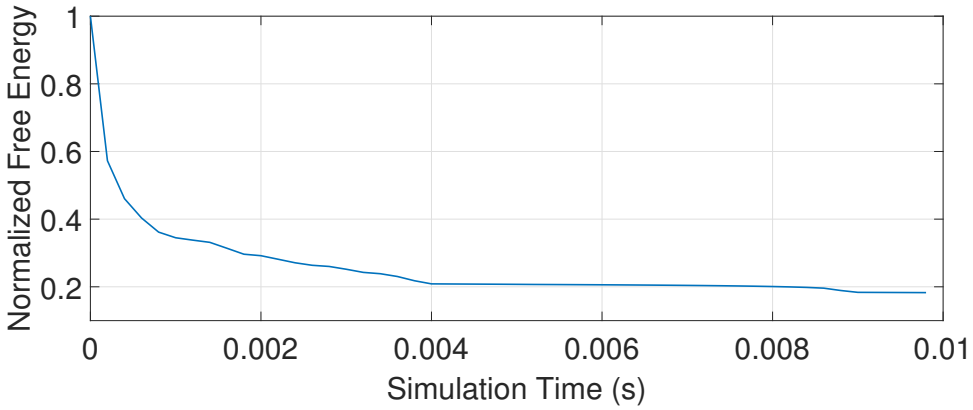

(b) Normalized free energy decay.

Figure 3.6: Quantities of interest of the spinodal decomposition simulations.

After assessing our methods and methodology, schemes of space and time adaptivity can be made to optimize the performance of the simulations.

Chapter 4

Preliminary studies

The Cahn-Hilliard equation can be coupled to phase-field equations to model multiflow simulations. Both Cahn-Hilliard and Allen-Cahn equations can be used for this purpose, except that the Allen-Cahn equation requires the use of Lagrangian multipliers to force the mass conservation property that does no exist in its pure formulation (VASCONCELOS *et al.* [49]). The Cahn-Hilliard equation properly conserves mass and presents energy decay, being naturally suitable for this coupling (GURTIN *et al.* [50]). However, the complex structure of the Cahn-Hilliard equation requires special attention when being numerically modelled, demanding large computational effort. In this section we assess a more complex situation where this equation is present to motivate our discussion in optimizing the modelling of the Cahn-Hilliard equation.

4.1 Phase-field methods on fluid dynamics

In the context of the coupled phase-field-fluid-dynamics models, the scalar order parameter of the phase-field models characterize each component of the mixture and the behaviour of each component is dictated by a set of coupled nonlinear differential equations: a modified Navier-Stokes set of equations, that update the pressure and velocities of the mixture and the convective-Cahn-Hilliard equation - or the convective-Allen-Cahn equation equipped with a Lagrange multiplier - which updates the concentration of each component and track the interfaces. The first work to couple the phase-field methodology with the fluid dynamics equations to simulate two-phase flow of immiscible, viscous fluids was HOHENBERG and HALPERIN [51], which was brought into the framework of the nonlinear continuum mechanics by GURTIN *et al.* [50], proving to be thermodinamically consistent. From this point, several works developed different Navier-Stokes-Cahn-Hilliard coupling strategies, each with its advantages and drawbacks. The models - listed and organized by HOSSEINI *et al.* [52] - are as follow:

Table 4.1: Different Navier-Stokes-Cahn-Hilliard models for two incompressible flows.

Model	Variable density $\rho_f(\phi)$	Thermody -namically consistent	Admitting energy law	Sharp interface limit identifiable when $\epsilon \to 0$
Model H		✓	✓	✓
LOWENGRUB and TRUSKINOVSKY [53]	✓	✓	✓	✓
DING *et al.* [54]	✓			✓
BOYER [55]	✓			
SHEN and YANG [56]	✓	✓	✓	
ABELS *et al.* [57]	✓	✓	✓	✓

After the development of the Model H, LOWENGRUB and TRUSKINOVSKY [53] circumvented the variable density constraint existent in the model proposed by Halperin and Hohenberg, creating a model labeled as *quasi*-incompressible Navier-Stokes-Cahn-Hilliard. The mean velocity of a given particle of the mixture is mass averaged - or also described as barycentric velocity - such that $\rho_f(\phi)\mathbf{u} = \rho_{f1}\mathbf{u}_1 + \rho_{f2}\mathbf{u}_2$, where the indexes 1 and 2 represent the individual components of the mixture. This assumption leads to a non-divergence-free velocity. Even though it is one of the most complete models for the Navier-Stokes-Cahn-Hilliard coupling, according to HOSSEINI *et al.* [52], until recently there were no discrete schemes available being based on the full model. The difficulty in solving numerically this model lies, specially, in two reasons: the strong nonlinearity existent in the presence of the pressure p on the chemical potential μ and by the non-solenoidal velocity field for which no solution concept is available which avoids to determine the pressure p. DING *et al.* [54] and BOYER [55] created models based on the generalization of the Model H to enable the use of fluids with large density ratio. However, there is no energy law related to their models or proof that these models are thermodynamically consistent, since these properties present on Model H are achieved through the assumption of small density ratio. Both models rely on averaging the velocity field by the volume fraction of each component of the mixture, that is, the velocity is treated as volume averaged thus $\mathbf{u} = v_1\mathbf{u_1} + v_2\mathbf{u_2}$. SHEN and YANG [56] presented a model where the information of the components are merged in the parameters of the Navier-Stokes equations, such that the density of the mixture is described as $\rho_f(\phi) = \frac{\rho_{f1} - \rho_{f2}}{2}\phi + \frac{\rho_{f1} + \rho_{f2}}{2}\phi$ and the viscosity is $\mu_f(\phi) = \frac{\mu_{f1} - \mu_{f2}}{2}\phi + \frac{\mu_{f1} + \mu_{f2}}{2}\phi$. This model presents an energy law and proper thermodynamical treatment. ABELS *et al.* [57] recently derived a thermodynamically consistent generalization of the Model H for the case of variable density based on a solenoidal velocity field $\mathbf{u}$, fulfilling local and global

dissipation inequalities and leads to a sharp interface model when $\epsilon \to 0$.

In this work, we have implemented the Model H, a coupled system between the Cahn-Hilliard equation and the Navier-Stokes equations in a way that the capillary forces on the interface are modelled in function of the phase-field order parameter. The Model H relies on matched density fluids, that is, both components have the same densities, being the most simple model within this framework. The Navier-Stokes momentum equation inherited an extra elastic stress induced by interfacial surface tension, while the Cahn-Hilliard equation gained a convection term dependent of the flow velocity. The Model H momentum equation is:

$$\rho_f[\frac{\partial \mathbf{u}}{\partial t} + (\mathbf{u}\cdot\nabla)\mathbf{u}] = \nabla\cdot[\mu_f(\nabla\mathbf{u} + \nabla\mathbf{u}^T) - p\mathbf{I} - \lambda(\nabla\phi\otimes\nabla\phi)]. \tag{4.1}$$

After considering proper rearrangement for Eq. (4.1), according to SHEN and XIAOFENG [58] and GURTIN *et al.* [50], the Navier-Stokes-Cahn-Hilliard set of equations can be formulated as:

$$\rho_f[\frac{\partial \mathbf{u}}{\partial t} + (\mathbf{u}\cdot\nabla)\mathbf{u}] = \mu_f\Delta\mathbf{u} - \nabla\tilde{p} + \mu\nabla\phi, \tag{4.2}$$

$$\nabla\cdot\mathbf{u} = 0, \tag{4.3}$$

$$\frac{\partial\phi}{\partial t} + \mathbf{u}\cdot\nabla\phi = M(\phi)\Delta\mu, \tag{4.4}$$

$$\mu = \Psi^{'} - \lambda\Delta\phi, \tag{4.5}$$

with $\tilde{p} = p - \dfrac{\lambda}{6}|\nabla\phi|^2 + \Psi(\phi)$.

4.2 The Cahn-Hilliard-Navier-Stokes coupling

The finite element methodology using the Galerkin method to a general partial differential equation is described in chapter 3.1. However, the use of finite element in transport problems involving convective terms and/or viscous incompressible flows requires certain attention and therefore needs further stabilization. There are two major reasons for stabilizing the incompressible Navier-Stokes equations and the convective Cahn-Hilliard equation when using the finite element method: First, the Galerkin method leads to central approximations of the convective terms and is thus not optimal when convection dominates diffusion (the viscosity effects), that is for high Reynolds number flows when modelling the incompressible Navier-Stokes momentum equation (DONEA and HUERTA [7]). This is also applicable to the scalar convection-diffusion-reaction equation with high Péclet number. The second problem is that the stability of the Galerkin method applied to the incompressible Navier-Stokes equations depends on satisfying of the Ladyzhenskaya-Babuška-Brezzi (LBB) condition. The following sections describe each of this issues,

how to fix their instabilities and how to derive the final finite element model for the incompressible Navier-Stokes equations.

4.3 Velocity and pressure coupling

The Navier-Stokes equations for an incompressible flow can be defined as:

$$\rho_f \left[\frac{\partial \mathbf{u}}{\partial t} + (\mathbf{u} \cdot \nabla)\mathbf{u} \right] - \mu_f \Delta \mathbf{u} + \nabla p = \mathbf{b} \qquad \text{in } \Omega \times [0, T], \tag{4.6}$$

$$\nabla \cdot \mathbf{u} = 0 \qquad \text{in } \Omega \times [0, T], \tag{4.7}$$

$$\mathbf{u} = \mathbf{u_D} \qquad \text{in } \Gamma_D \times [0, T], \tag{4.8}$$

$$-p\mathbf{n} + \mu_f (\mathbf{n} \cdot \nabla)\mathbf{u} = u_T \qquad \text{in } \Gamma_N \times [0, T], \tag{4.9}$$

$$\mathbf{u}(\mathbf{x}, 0) = \mathbf{u_0}(\mathbf{x}) \qquad \text{in } \Omega, \tag{4.10}$$

where ρ_f is the fluid density, $\mathbf{u}$ is the fluid convective velocity, μ_f is the kinematic viscosity, p is the pressure and $\mathbf{b}$ is the volume force per unit mass of fluid. $\mathbf{u}_D$ and $\mathbf{u}_T$ are the boundary conditions prescribed on the boundaries Γ_D and Γ_N, respectively, and $\mathbf{u}_0$ are the initial conditions.

Equation (4.7) is the incompressibility constraint of the fluid, being the consequence of the fact that in an incompressible continuum the rate of change of the mass density following the motion is zero. This incompressibility constraint causes unstable behaviour in the finite element method when an inappropriate combination of element interpolation functions for the velocity and pressure is employed. As a consequence, instabilities in the pressure field may appear, and this is independent of the Reynolds number. The Ladyzhenskaya-Babuška-Brezzi condition - also known as LBB condition or inf-sup condition - is stated as: The existence of a stable finite element approximate solution $(\mathbf{u}^h, p^h)$ to the steady Stokes problem or the incompressible Navier-Stokes equation depends on choosing a pair of spaces V^h and Q^h, such that the following discrete inf-sup condition holds:

$$\inf_{q^h \in Q^h} \sup_{w^h \in W^h} \frac{(q^h, \nabla \cdot w^h)}{||q||_0 ||w^h||_1} \geq \theta > 0, \tag{4.11}$$

where θ is independent of the mesh size. Several pair of elements have been proved to be within this context, being suitable for modelling the incompressible Navier-Stokes equation. In this study we consider the Taylor-Hood (TAYLOR and HOOD [59]) pair of elements, where the pressure elements and velocity base functions are, respectively, linear and quadratic piecewise polynomials.

4.4 Convection dominated flows

As shown on the previous section, the Cahn-Hilliard equation inherits a convection term after the coupling with the Navier-Stokes equation. That is, the altered Cahn-Hilliard equation has now a convection-diffusion-reaction form.

It is known that the traditional Galerkin formulation can lead to global spurious oscillations on high Reynolds number flows while solving the Navier-Stokes equation (DONEA and HUERTA [7]). It is also described in JOSHI and JAIMAN [60] that diffusion-reaction equations with reaction dominated flows and convection-diffusion equations with advection dominated flows reveal the same behaviour. Since this study uses the finite element method for numerical approximation of the described PDEs, additional stabilization techniques will be required.

Many stabilization techniques have been developed in the past decades, such as the Streamline Upwind Petrov-Galerkin method (BROOKS and HUGHES [61]), the Galerkin Least Squares method (HUGHES *et al.* [62]) and the Subgrid Scale method (HUGHES [63]). All methods rely on a different way to model the weight functions. On JAIMAN and JOSHI [60], a new stabilization technique is proposed for the convection-diffusion-reaction equation. We implemented this method and compared to the others previously cited. On Appendix A we assess some formulations for different situations for the convection-diffusion-reaction equation.

4.5 Numerical validation

The two kissing bubbles example is a situation where two touching droplets of a given fluid are immerse in a different immiscible fluid. This example simulates the coalescence of two similar phases and evaluate the interfacial forces. To simulate the two kissing bubbles example, we consider the following initial condition, which is described by Fig. 4.1

$$\begin{aligned}\phi(x,y,0) =& \tanh[200(x-0.4)^2+200(y-0.5)^2-\sqrt{2}]+ \\ & \tanh[200(x-0.6)^2+200(y-0.5)^2)-\sqrt{2}]-1. \end{aligned} \tag{4.12}$$

For the time integration of the incompressible Navier-Stokes equation, we considered a semi-implicit fractional-step projection method proposed by CHORIN [64] and TEMAM [65]. The principle of this method is to evaluate the velocity and pressure fields separately through the computation of an intermediate velocity, which is then projected onto the subspace of the solenoidal vector functions, forcing the velocity to become divergence-free. We implemented the SUPG stabilization method for both the incompressible Navier-Stokes and convective Cahn-Hilliard equations in our simulations.

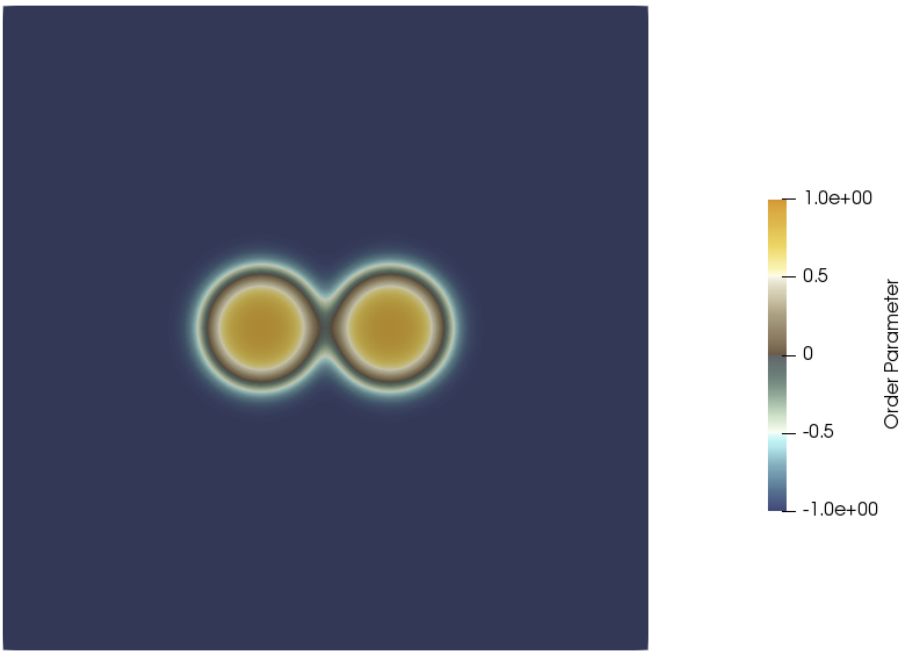

Figure 4.1: Initial condition for the two-kissing bubble simulation.

This simulation represents a decoupled multiphysics system, where both equations are updated separately and evaluated separately. We compare our results with the ones seen on VASCONCELOS *et al.* [49], with presented similar behaviour. The convective Cahn-Hilliard equation is solved implicitly with a nonlinear solver while the modified incompressible Navier-Stokes equation is solved with a semi-implicit Chorin-Temam projection method. The two kissing bubbles simulation was solved on a Intel Core i5-3230M 2.60GHz with 8 GB of RAM for approximately 4 days. Most of the time spent on the simulation was solving the nonlinear system originated from the Cahn-Hilliard equation. This reinforces the idea that the optimization of the numerical scheme used in the phase-field equations is essential for simulating the desired physical phenomena in feasible time.

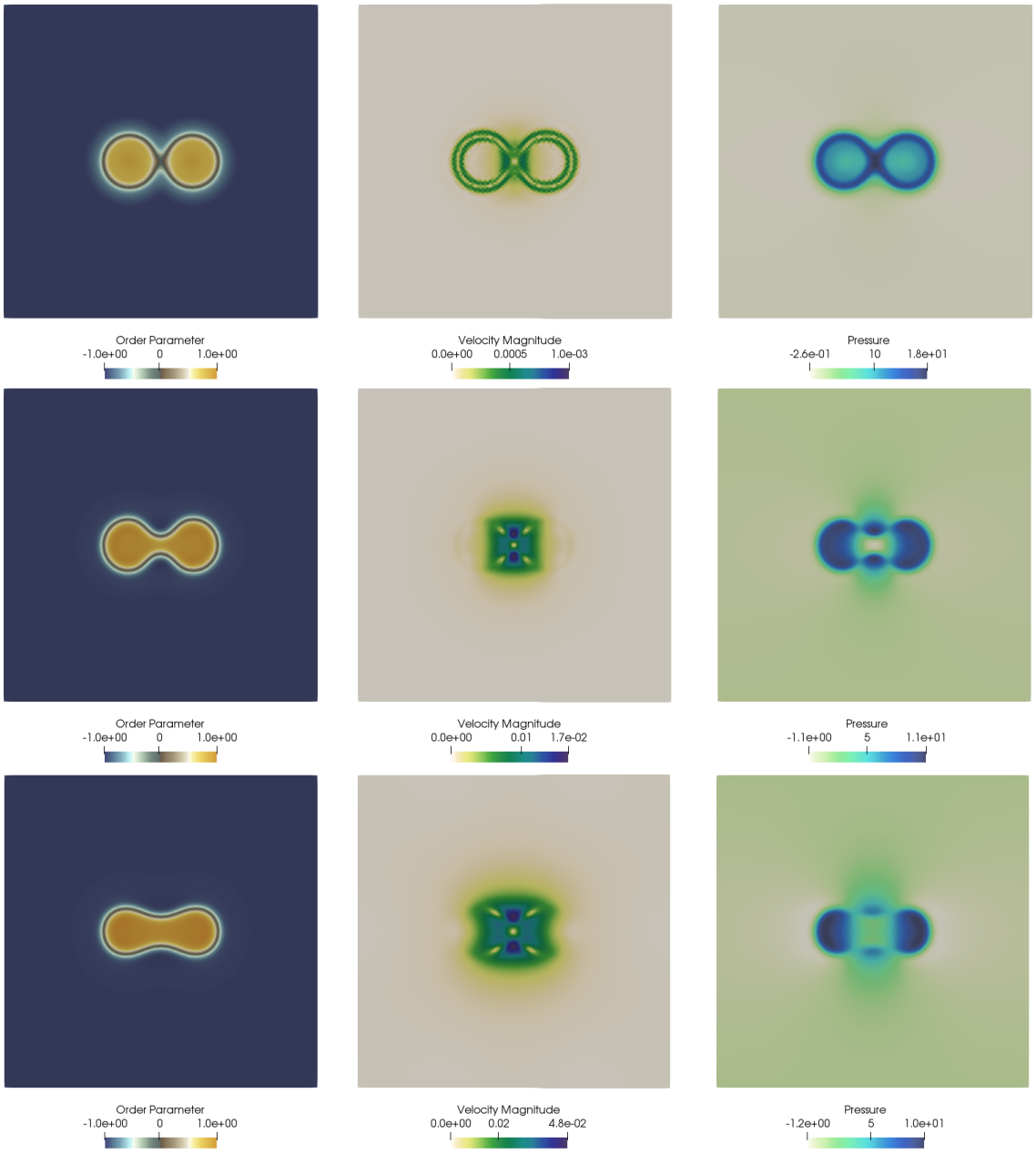

Figure 4.2: Early stages of the merging droplets. Velocity fields present smaller magnitudes and pressure field points the potential direction of the fluid motion.

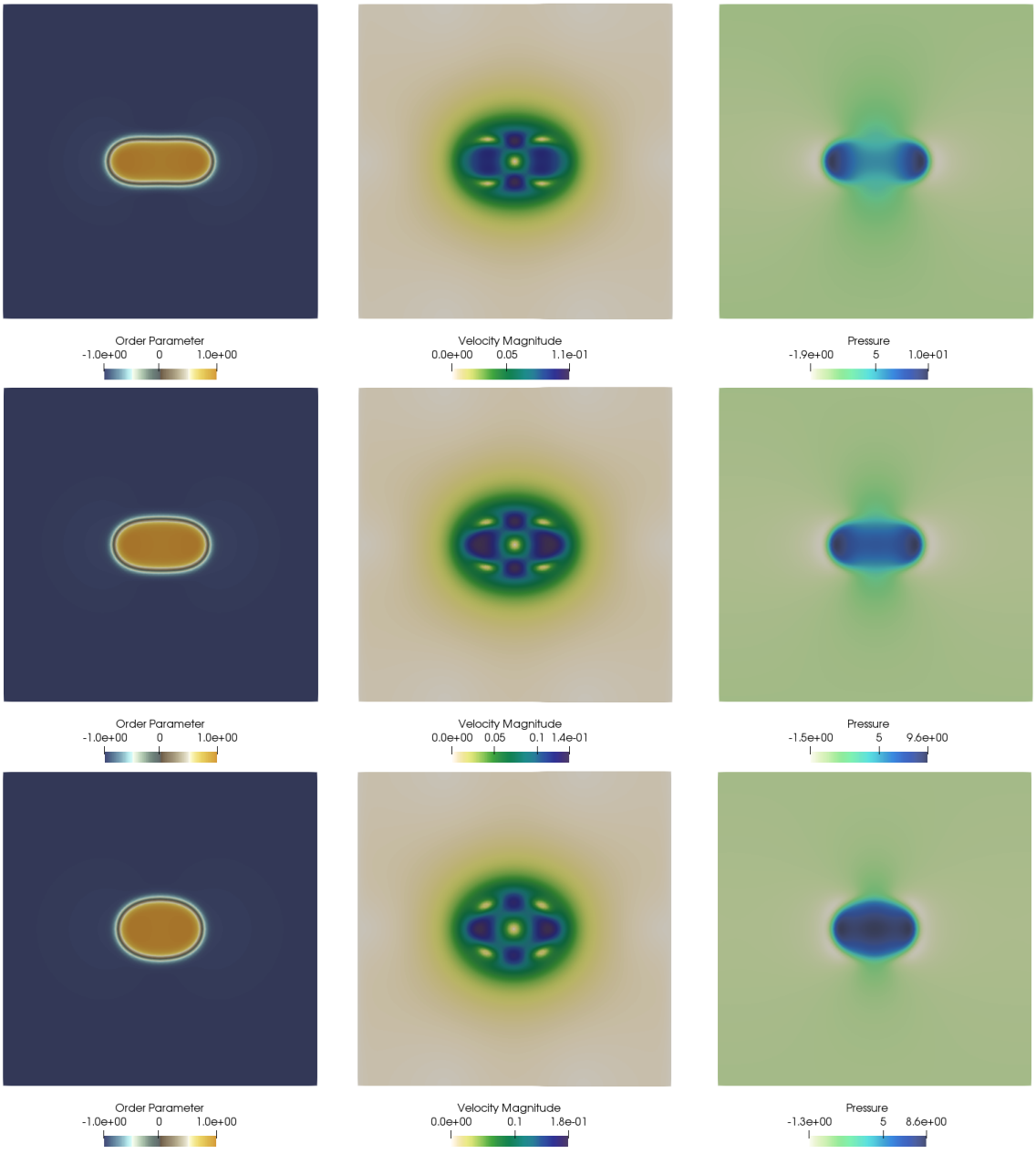

Figure 4.3: Intermediate stages of the merging droplets. Velocity fields present larger magnitudes in comparison to the early stages. The two bubbles now are a single phase mass.

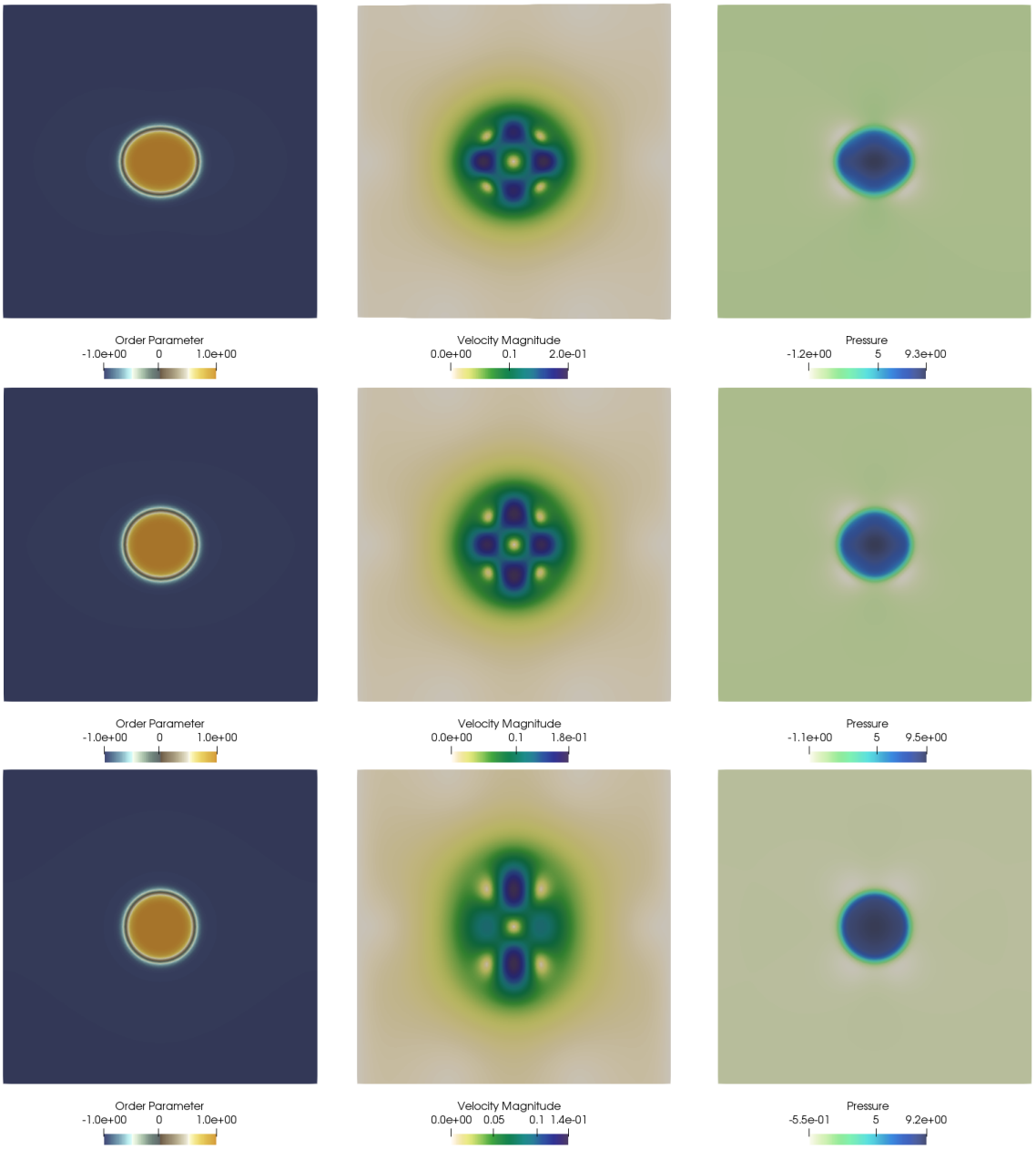

Figure 4.4: Later stages of the merging droplets. Velocity fields begins to reduce its magnitudes while the bubble reach its circular form.

Chapter 5

Adaptivity Schemes

Phase-field simulations involve a connection between different scales and this can represent a gap between time and space scales. The computational cost of a spinodal decomposition simulation using the Cahn-Hilliard equation is high, since it is a time-dependent nonlinear PDE that requires long time simulations with the presence of fast dynamics on the early stages, requiring small time step sizes. In this chapter, we will discuss space and time adaptivity strategies for the Cahn-Hilliard equation to optimize the computational cost without compromising the accuracy of the fixed time step and mesh results. Each section deals with a separate subject that will compare the results with the simulation presented on section 3.6.

5.1 Time adaptivity

The choice of a proper time integration method and time step for the Cahn-Hilliard equation is a difficult task, since the equation, in several physical situations, have different time scales in their nature, creating a conflict between accuracy and performance. For example, the initial phase of the spinodal decomposition is dictated by fast dynamics, requiring small step sizes while the latter stages reveal slow dynamics, allowing large time steps. Thus, to improve the efficiency of the computations, a time adaptivity scheme is often used to automatically change the time step size to capture both fast and slow dynamics of the Cahn-Hilliard equation, improving the performance of the simulations without any accuracy loss.

Studies in the literature discuss time adaptivity schemes for the Cahn-Hilliard equation. Some schemes rely on the Cahn-Hilliard physical nature (GUILLÉN-GONZÁLEZ and TIERRA [66], ZHANG [67]), where the adaptivity scheme is based on the variation of the free energy functional. Several studies adopted different approaches where the proposed schemes are based on a simple time step controller, seen in GÓMEZ and HUGHES [38] WODO and GANAPATHYSUBRAMANIAN [45], CUETO-FELGUEROSO and

PERAIRE [68], VIGNAL et al.[17]. In this study, our approach is to assess different controllers with a recent error estimation scheme by using the linear feedback control theory in a numerical context.

5.1.1 The control theory on adaptive time-stepping

The Cahn-Hilliard equation is a dynamical system of the form:

$$\dot{\phi} = F(\phi), \qquad \phi(\mathbf{x}, 0) = \phi_0, \tag{5.1}$$

where $\phi \in \mathbb{R}^{nsd}$ and $F : \mathbb{R}^{nsd} \to \mathbb{R}^{nsd}$ is a smooth Lipschitz map. Since the time integration method used in this study is a one-step method, considering a step size Δt, there is a map $\Phi : \mathbb{R}^{nsd} \to \mathbb{R}^{nsd}$ such that:

$$\phi_{n+1} = \Phi(\phi_n), \qquad \phi(\mathbf{x}, 0) = \phi_0. \tag{5.2}$$

Equation (5.2) is a discrete-time dynamical system that approximates Equation (5.1). It is possible to use the same approach for an additional map $\Xi : \mathbb{R} \to \mathbb{R}$ to vary the step size:

$$\Delta t_{n+1} = \Xi(\Delta t_n). \tag{5.3}$$

The map Ξ uses information about the numerical solution ϕ_n when defining the new step size (Δt_{n+1}) while the map Φ is based on the time step Δt. An adaptive time–stepping method can be expressed as the following interactive recursion:

$$\phi_{n+1} = \Phi(\phi_n), \tag{5.4}$$

$$\Delta t_{n+1} = \Xi(\Delta t_n). \tag{5.5}$$

Most of the adaptive time-step schemes are based in the interactive recursion seen on Equations (5.4) and (5.5). It is assumed that the relation between the error and the step size is asymptotic, that is:

$$r_n = |\zeta_n| \Delta t_n^{\kappa}, \tag{5.6}$$

where r_n is the norm of the local error estimate, $|\zeta_n|$ is the norm of the principal error function, and κ is related to the order of accuracy of the time integration method. In our case, the principal error function can be viewed as a disturbance in the system, such as a Newton solver residual and other properties of the Cahn-Hilliard equation. Also the integration method employed is second-order accurate, so $\kappa = 2$. From the assumption seen in Eq. 5.6, we can observe that $r_n \to 0$ if $\Delta t \to 0$.

The idea behind the use of control theory on adaptive time-stepping is that the map Ξ controls an estimated numerical error within a prescribed tolerance TOL. The recursion

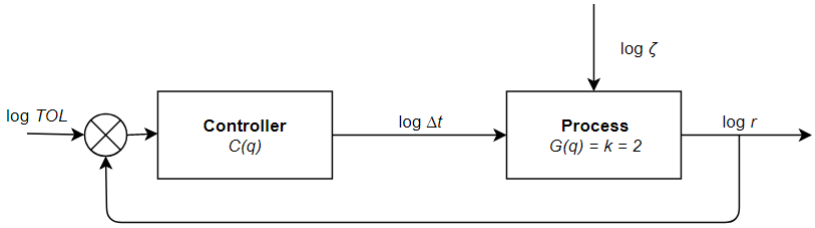

Figure 5.1: Adaptive time-stepping viewed as a feedback control system. Adapted from SÖDERLIND [5].

can be translated into a closed loop, a common dynamic structure in the control theory. We can split the map Ξ into two parts: the process transfer function $G(q)$ and the control transfer function $C(q)$, where q is the forward shift operator, considering the process after the $z - transform$ (SÖDERLIND [69]). In our context, the process transfer function is responsible for evaluating the Cahn-Hilliard equation and its local error during the present time-step, while the control transfer function can be viewed as the transfer function that evaluates the next time step considering the error obtained from $G(q)$ and the initially prescribed tolerance TOL. The adaptive time-stepping closed loop can be seen in Figure 5.1. The interactive recursion describes the interaction between the process and the controller:

$$\log r_n = G(q) \log \Delta t_n + \log |\zeta_n|, \tag{5.7}$$

$$\log \Delta t_{n+1} = C(q) \cdot (\log TOL - \log r_n). \tag{5.8}$$

However, the process transfer function can be obtained by the asymptotic assumption presented on Equation 5.6. This leads to the following closed loop dynamics [69]:

$$\log r_n = R_{TOL}(q) \log TOL + R_\zeta(q) \log |\zeta|, \tag{5.9}$$

$$\log \Delta t_{n+1} = H_{TOL}(q) \log TOL + H_\zeta(q) \log |\zeta|, \tag{5.10}$$

where the stepsize transfer map $H_\zeta(q)$ and the error transfer map $R_\zeta(q)$ are given by:

$$H_\zeta(q) = -\frac{C(q)}{1 + \kappa C(q)}, \qquad R_\zeta(q) = -\frac{1}{1 + \kappa C(q)}. \tag{5.11}$$

The recursion formed by Equations (5.9) and (5.10) expresses how the two inputs: the prescribed tolerance $\log TOL$ and the disturbance $\log |\zeta|$ influence the two outputs: the error estimate $\log r$ and the stepsize $\log \Delta t$. The stepsize transfer map $H_\zeta(q)$ and the error transfer map $R_\zeta(q)$ can be interpreted as digital filters implying that the stepsize sequence $\log \Delta t$ is considered to be obtained through digital signal processing of the external disturbance $\log |\zeta|$ (SÖDERLIND [69]).

In this sense, the use of the linear feedback control theory on step size adaptivity is translated into: given a present time step t_n, choose a future time step Δt_{n+1} such that

the local error of the present time step r_n is controlled within a given tolerance TOL by a controller whose properties and tuning are defined by $C(q)$. Besides from the expectancy of reducing the number of linear/nonlinear systems to be solved, the control theory provides smoother step size sequences, which improves the solution evolution (SÖDERLIND [70]), improved computational stability and a regular, tight tolerance proportionality.

5.1.2 Error estimation

We consider an error estimation where the solutions at t_n and t_{n-1} are stored and the error is estimated *a posteriori* by extrapolation by a lower-order time integration method, since the solution t_{n+1} is obtained with a second order scheme. This method is proposed by VIGNAL *et al.* [17]. This estimation is done through variable step-size backward differentiation, where the error obtained in the lower-order method is controlled. In this work, we consider the lower-order method to be the backward-Euler method. Therefore, the local truncation error of the backward-Euler method is:

$$\tau^{BE}(t_{n+1}) = -\frac{\Delta t^2}{2}\phi^{''}(t_{n+1}) + O(\Delta t^3). \tag{5.12}$$

Given the stored solutions ϕ_{n+1}, ϕ_n and ϕ_{n-1} at times t_{n+1}, t_n and t_{n-1} respectively and neglecting the effects of the $O(\Delta t^3)$ terms, equation (5.12) can be approximated by the variable step-size backward difference formula. So the error estimation is now:

$$\mathbf{E}_{n+1} = -\frac{1}{\eta}\phi^h_{n+1} + \frac{1}{\eta - 1}\phi^h_n - \frac{1}{\eta(\eta-1)}\phi^h_{n-1}, \tag{5.13}$$

where $\eta = (\Delta t + \Delta t_p)/\Delta t$, with $\Delta t = t_{n+1} - t_n$ and $\Delta t_p = t_n - t_{n-1}$.

With the error function, the weighted local truncation error (WLTE) can be written as:

$$r = \sqrt{\frac{1}{n_{nodes}}\sum_{i=1}^{n_{nodes}}\left(\frac{\mathbf{E}^{(i)}_{n+1}}{\tau^{abs} + \tau^{rel}\text{max}(|\phi^{(i)}_{n+1}|, |\phi^{(i)}_{n+1} + \mathbf{E}^{(i)}_{n+1}|)}\right)^2}, \tag{5.14}$$

where τ^{abs} and τ^{rel} define tunable absolute and relative tolerances, respectively, and the index $i = 1, 2, ...n_{nodes}$ refers to the nodal index.

The weighted local truncation error r is used to control the error at each time step. By definition, values of $r \leq 1$ mean that the local truncation error is within the user-prescribed tolerances. In this case, the step just taken can be accepted and the time integration can move forward with either the same or a larger time step size. On the contrary, values of WLTE larger than one imply unacceptable errors, that is, the step taken should be rejected and retaken with a smaller time step size, since the error r_{n+1} becomes larger and therefore decreases the new time step Δt_{n+1} in this case.

Table 5.1: Controllers parameters.

κ_D	κ_I	κ_D	κ_T	Controller
0.0	0.5	0.0	0.0	Integral (I)
0.075	0.175	0.01	0.0	PID
0.333	0.333	0.0	1.0	PC11

5.1.3 Timestep controllers

There are several timestep controllers in the literature and many ways to classify them (SÖDERLIND [5]). In this study, we consider three controllers: an integral controller, a PID controller, and a predictive controller. The integral controller is the simplest used in time adaptivity and controls the relationship between the error in the present and past time. This simplicity is known to grant the integral controller a large number of rejected steps according to CUETO-FELGUEROSO and PERAIRE [68]. The PID controller has three controlling terms - proportional, integral and derivative - that adjust the time step with respect to the last three time steps. The predictive controller is the most indicated controller for time adaptivity in stiff equations (SÖDERLIND [70]) and has a different structure when compared to the other two controllers. The three controllers can be written as:

$$\Delta t_{n+1} = \rho \left(\frac{r_n}{r_{n+1}} \right)^{\kappa_P} \left(\frac{1}{r_{n+1}} \right)^{\kappa_I} \left(\frac{r_n^2}{r_{n+1} r_{n-1}} \right)^{\kappa_D} \left(\frac{\Delta t_n}{\Delta t_{n-1}} \right)^{\kappa_T} \Delta t_n, \tag{5.15}$$

where the parameter $\rho = 0.9$ for all methods is a safety factor used to smooth the steptime growth. The parameters κ_P, κ_I, κ_D and κ_T for each controller are represented in Table 5.1. To avoid tuning the parameters, which can be very time consuming, the parameters for the I controller, the PID controller and the PC11 controller were taken respectively from SÖDERLIND [70], VALLI et al. [71] and AHMED and JOHN [72].

Remark: Although the use of time adaptivity schemes based on the linear feedback control theory has not yet been explicitly mentioned in the Cahn-Hilliard literature, the integral controller has been used in the present context in several works such as CUETO-FELGUEROSO and PERAIRE [68], GÓMEZ and HUGHES [38], VIGNAL et al. [17] WODO and GANAPATHYSUBRAMANIAN [45]. Even when the PID controller has been used in the Cahn-Hilliard context (CUETO-FELGUEROSO and PERAIRE [68]), the integration method used for the PID error estimation is not guaranteed to be energy stable. Also, the error estimation employed was based on solution norms of different time integration methods with different orders of accuracy. This error estimation requires the calculation of the same step twice and therefore can be time-consuming. In the present work, we employ an error estimation method based on extrapolation that avoids computing the same time step twice.

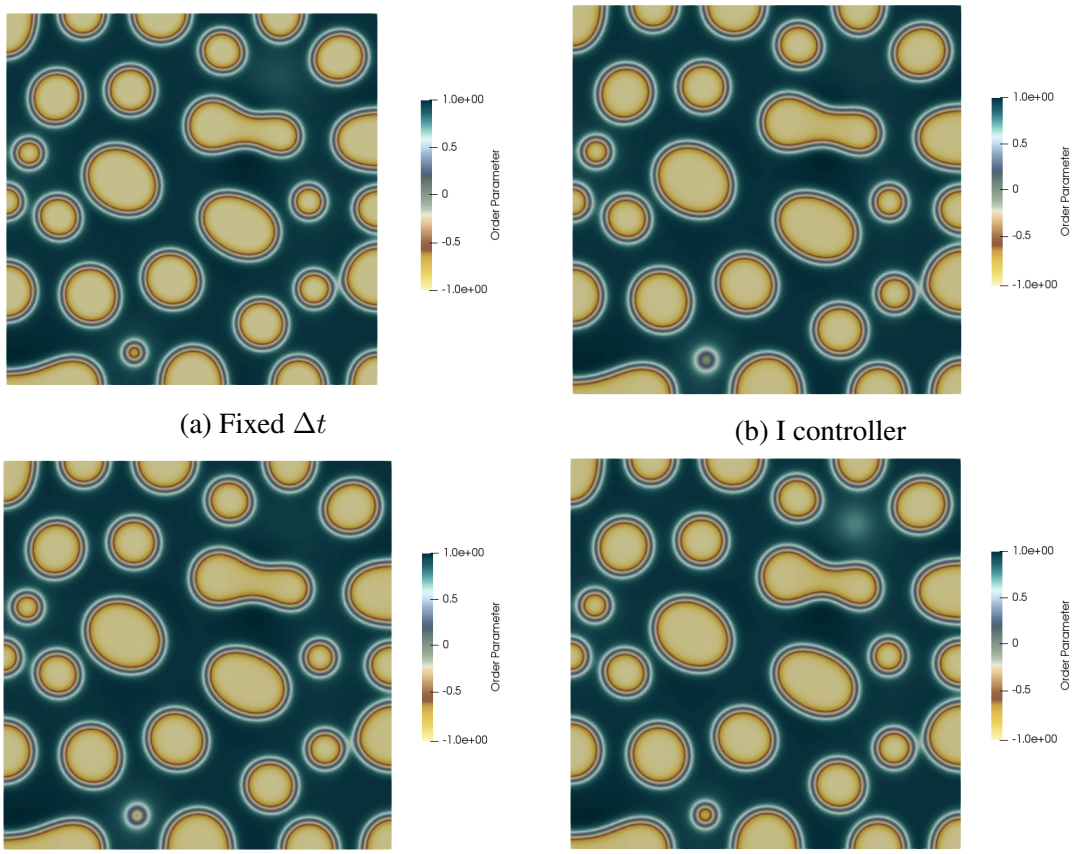

(a) Fixed Δt

(b) I controller

(c) PID controller

(d) PC11 controller

Figure 5.2: Simulations at $t = 0.006s$ using different adaptivity strategies revealing that there is no significant difference between each simulation.

5.1.4 Numerical validation

Numerical simulations are made to validate the time adaptivity strategy. Four constant mobility phase separation simulations are made: one for each controller and the fixed time step simulation is used to validate the spatial adaptivity scheme. We aim to compare the frames in all simulations to check if they all represent the same physical stage. The same fixed mesh simulation used in section 3 is employed in this validation. For our simulations, we consider $\tau^{abs} = \tau^{rel} = 10^{-4}$ and the initial time step $\Delta t_0 = 10^{-9}$.

Figure 5.2 show all simulations at the same instant. Even that it is possible to see small differences between simulations, there is no significant loss of accuracy. It is also essential to observe that during the early stages of the simulation, the adaptive time step is much smaller than the fixed time step, revealing that the adaptive strategy is inefficient for a short period. Figure 5.3 shows how many time steps are needed for each method to reach the point where the fixed time step is no longer more efficient. The integral controller method reached the fixed time step on step number 891, PC11 did it in step 937 while PID did it in step 1197. It is expected that the PID controller would behave more conservatively, since its formulation consists of evaluating the error on different

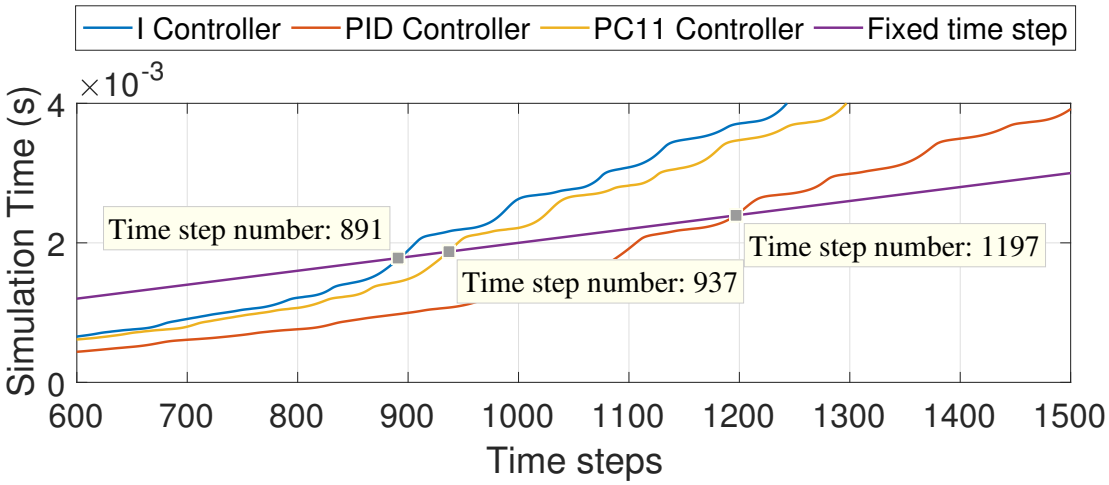

Figure 5.3: Comparison between physical simulation time between the fixed time step and the proposed controllers. The adaptive time stepping scheme with the given tolerance takes around 1000 time steps to reach the fixed time step simulation in physical time.

times, making it a more rigid controller than the others. Time step adaptivity facilitates to reach the steady-state of the Cahn-Hilliard equation. In our simulations, the steady-state is reached at around $t = 0.7$s. To reach the steady-state using the fixed time step scheme, considering that $\Delta t = 2 \times 10^{-6}$, it would be necessary 325×10^3 time steps, while using the time step adaptivity, it is reached within around 5000 time steps.

Table 5.2 shows a comparison of the results. All nonlinear solutions converged, that is, the growth of the time step adaptivity is sufficiently smooth to prevent any non-convergence, thanks to the prescribed tolerance values. All methods significantly improved the spinodal decomposition simulation, since it is possible to reach larger simulation times with a lesser number of steps. It can be said that the methods do not show considerable differences between them since they all reached the steady-state with approximately 5000 time steps. The last column in the table shows that the PC11 is the method that solved less nonlinear systems. The PID controller solved the most, and it is the most conservative. The integral controller contained only the error in the present time e_{n+1} and, therefore, had less control over the growth of the time steps, presenting more rejected steps over the other methods. The fixed time step simulation does not need any strategy to reject steps.

We can conclude that the use of time adaptivity schemes for the Cahn-Hilliard equation is better for long simulations. The error controllers used proved to be reliable in the sense that no inaccurate solutions are obtained when compared to the fixed time step while providing the desired performance. The comparison between the methods suggests that the PC11 behaved slightly better in the spinodal decomposition simulations. However, here we only want to show the necessity of using a time adaptivity scheme instead of a fixed time step scheme for long time simulations. The results shown suggest that this is a

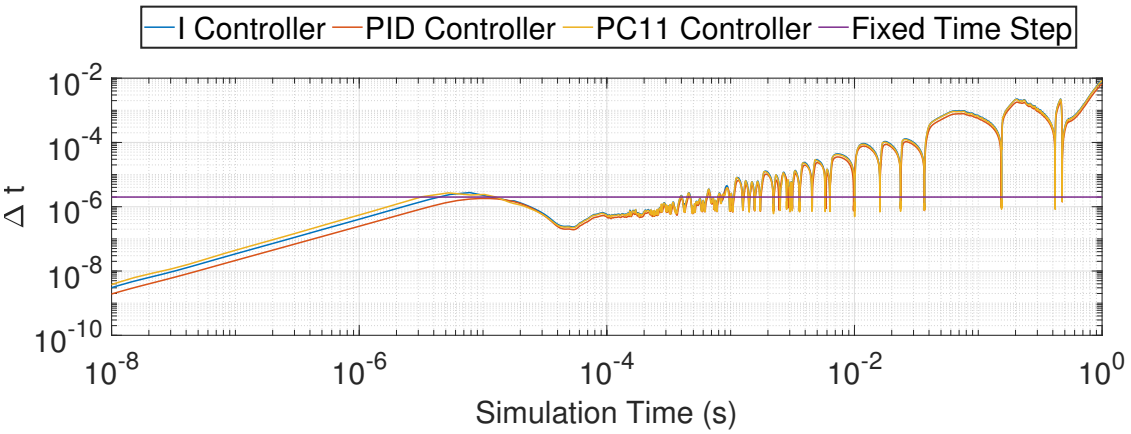

Figure 5.4: Behaviour of the time step Δt during the simulations. The time step is kept around $O(10^{-6})$ in the initial stages where the interfaces arise. In the mid and late stages, where the dynamics are mostly dictated by mobility and shrinkage, the time step can reach larger values. The time step is reduced to $O(10^{-6})$ when the Ostwald Ripening phenomenon is observed, that is, a given portion of a phase shrinks until its mass is completely transported to a larger portion. This phenomenon reveals fast dynamics thus reducing the time step size. It is also observable that all the simulations represent the same physics since all curves reveal time step size reduction in the same simulation time.

Table 5.2: Results for the time adaptivity schemes for each time step controller.

Method	Time steps	Simulation time (s)	Rejected steps	Nonlinear systems solved
Fixed Δt	5000	0.01	-	5000
I	4415	1.00	272	4687
PID	5307	1.00	102	5409
PC11	4516	1.00	75	4591

good choice.

5.2 Space adaptivity

It is known that the Cahn-Hilliard equation requires a proper discretization in the interfacial domain to guarantee the accuracy of the boundary motion (WODO and GANAPATHYSUBRAMANIAN [45]). However, the bulk domain (defined by plain phases) does not need to be numerically detailed, allowing the use of a coarser discretization in these regions. Considering a nonlinear set of equations on a long time simulation, the reduction of degrees of freedom in the bulk domain can be a huge improvement in the computational cost of the simulation, without compromising its accuracy and robustness.

Several papers have used spatial adaptivity to improve the performance of the Cahn-

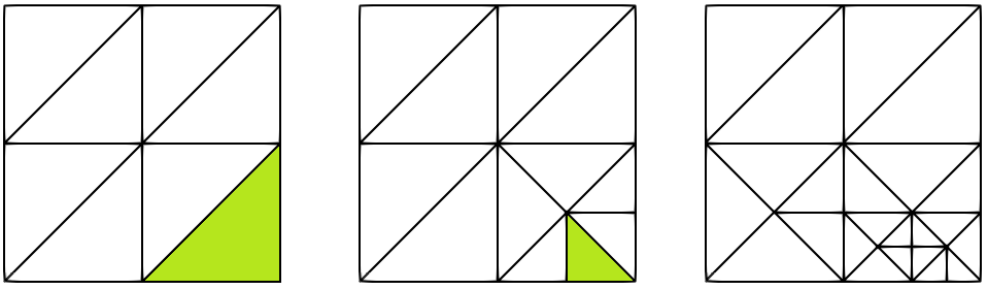

Figure 5.5: Triangular mesh refinement procedure using the bisection method. The green element is marked for refinement since its value η_{el} is greater than a prescribed tolerance at each iteration.

Hilliard simulations varying in refinement criteria, procedure or numerical method. In the Cahn-Hilliard numerical literature, two refinement criteria are often used: the value of the order parameter close to the value defined for the interfaces or its gradient (CENICEROS and ROMA [73]).

5.2.1 Spatial error indicators

Error estimators and indicators of different degrees of complexity and computational cost can be used to drive adaptive simulations. We can highlight residual, interpolation-based, flux jump, patch recovery and adjoint-based dual estimators (CAREY [74]). In this section, we consider two error indicators and compare their behaviors. To setup the nomenclature of our refinement procedure, we consider some definitions. Our non-degenerate family of simplices meshes $\{\mathcal{T}_z\}_{z\in\ddagger}$ are obtained by local refinements of a reference coarse mesh, denoted hereafter by $\mathcal{T}^{\text{coarse}}$ at every iteration z. At the other end, we consider a reference fine mesh, denoted hereafter by $\mathcal{T}^{\text{fine}}$, assumed to resolve all the scales of the solution, meaning that its characteristic mesh length is capable of capturing the diffuse interface thickness according to equation (2.7). So each member of the family of meshes $\{\mathcal{T}_z\}_{z\in\ddagger}$ is a mesh with characteristic length between $\mathcal{T}^{\text{coarse}}$ and $\mathcal{T}^{\text{fine}}$. The specification of $\mathcal{T}^{\text{coarse}}$ and $\mathcal{T}^{\text{fine}}$ are problem dependent, and will be given in the numerical validation section. We consider a spatial error vector $\eta^2 = \{\eta_e^2\}, e = 1, 2, ..., nel$, which is the number of elements in the current mesh.

Initially, we use a modified error indicator procedure based on the residual of the Cahn-Hilliard equation, proposed by BAÑAS and NÜRNBERG [75]. This error indicator have been adjusted to fit our time integration method. The authors proposed two error indicators based on each equation of the Cahn-Hilliard nonlinear system (3.12). However, only one of these equations have practical computational applications and, after preliminary numerical evaluations, we observed that the same behaviour occurred in our simulations. Therefore, considering the defined spaces in Eq. (3.7), the discrete residual of the second equation in (3.12), $R_\mu^h \in S_t^h$ is defined as:

$$R_{\mu}^{h} = (q^{h}, \mu_{n+1}^{h}) - (q^{h}, \tilde{\Psi}^{'}) - \epsilon^{2}(\nabla q^{h}, \nabla\{\phi\}) \quad \forall q^{h} \in W^{h}. \tag{5.16}$$

The first local error indicator considered, is then,

$$\eta_{e}^{2} = \left|\left| h_{el}\left(\mu_{n+1}^{h} - \tilde{\Psi}^{'} - R_{\mu}^{h}\right)\right|\right|_{L_{2}(\Omega^{e})}^{2} + \epsilon^{2}\sum_{s=1}^{3}||h_{s}^{1/2}[\nabla\{\phi\}]_{s}||_{L_{2}(s)}^{2}, \tag{5.17}$$

where h_{el} is the element size, Ω^{e} is the element domain, s is the triangle edge, h_{s} is the edge length, and $[\nabla\{\phi\}]_{s} = (\nabla\{\phi\})^{+}\cdot\mathbf{n}^{+} + (\nabla\{\phi\})^{-}\cdot\mathbf{n}^{-}$ is the jump of the gradient of the average phase field across the inter element boundary s, and $\mathbf{n}$ is the unit normal vector to s. The superscripts $+$ and $-$ indicate that the vectors are evaluated in the positive and negative directions of the facet s, respectively. The main difference between this procedure and the original presented in BAÑAS and NÜRNBERG [75] is that we do not consider any approximation of the free energy density function besides the Taylor's series expansion presented in Eq. (3.13). The first term on Eq. (5.17) refers to the residual of the nonlinear system second equation while the second term takes into account the average phase field jump.

The second procedure tested is a simple phase-field flux jump. In this case, the error indicator is:

$$\eta_{e}^{2} = \sum_{s=1}^{3}||h_{s}^{1/2}[\nabla\phi_{n+1}^{h}]_{s}||_{L_{2}(s)}^{2}, \tag{5.18}$$

where $[\nabla\phi_{n+1}^{h}]_{s} = (\nabla\phi_{n+1}^{h})^{+}\cdot\mathbf{n}^{+} + (\nabla\phi_{n+1}^{h})^{-}\cdot\mathbf{n}^{-}$.

In both cases the global error indicator can be expressed as:

$$\eta_{\Omega} = \frac{||\eta^{2}||_{L^{2}}}{\sqrt{nel}} = \sqrt{\frac{\sum_{e=1}^{nel}\eta_{e}^{2}}{nel}}. \tag{5.19}$$

In this study, we aim to achieve the same total error with less degrees of freedom to increase the simulation efficiency. Thus the total error η_{Ω} of the adaptive meshes should not surpass the total error obtained in the fixed mesh simulations η_{Ω}^{Fixed} - evaluated from the solution on the mesh $\mathcal{T}^{\text{fine}}$ -, while the maximum norm $||\eta||_{\infty}$ is responsible for flagging the elements that should be refined. The maximum norm is defined such that a given mesh should present local errors within a prescribed value and presents direct influence on the mesh generated.

The refinement procedure occurs as follows:

---

1. Solve the Cahn-Hilliard equation for the previous mesh (in case of initial step, the fine mesh $\mathcal{T}^{\text{fine}}$ is used)

2. Local error vector η^2 is calculated using equation (5.17) or (5.18) for every element in the mesh. Global error η_Ω is then evaluated.

3. If $\eta_\Omega > \eta_\Omega^{Fixed}$ or the present time step is defined for refinement:

   (a) While the target element size is not achieved or the maximum number of refinement iterations is reached:

      i. Project the solution onto the updated mesh $\mathcal{T}_z$ by interpolation (root mesh if it is the first iteration).

      ii. Loop over the cells in the current mesh and compare the local error of each element η_e with the maximum norm allowed for the error vector $||\eta||_\infty$.

      iii. Mark the cells that surpassed the maximum norm allowed for the mesh $||\eta||_\infty$.

      iv. Refine and update the mesh.

   (b) Interpolate the previous solution onto the created mesh.

4. Proceed to the nonlinear system solver and solve the present time step for the generated mesh.

The global error criterion defines the target element size to be the same used in the fixed mesh simulations. Nevertheless, in this study, we consider the target element size to have the exact same element size of the fixed fine mesh, prescribing the iterations needed to refine the mesh to achieve the same discretization used in the fixed mesh simulations. Thus the interfaces do not become more discretized than the fixed mesh case and the global error η_Ω is almost identical in both adaptive and fixed cases. It is important to mention that the refinement iterations z are not related to the nonlinear solver iterations. The refinement procedure takes place before solving the system for the time step $n + 1$. The mesh refinement procedure follows the bisection method (RIVARA [76]) which is a built-in function in the `FEniCS` framework. Figure 5.6 presents the behavior of the mesh refinement procedure for a given situation. In this section, for validation, the mesh refinement routine is called in every time step.

The interpolation procedure used to transfer the solution at each iteration of the mesh refinement routine is a built-in function on `FEniCS`. The solution ϕ^h is a linear combination of the nodal values and basis functions in the mesh. When transferring the solution to a different mesh, the function `interpolate` maps the nodes coordinates $\mathbf{x}_{new}$ and evaluates the solution $\phi^h(\mathbf{x}_{new})$ originating the nodal values for the new mesh. When this process is coupled to the bissection refinement procedure in linear elements, the generation of a new node in the median of a triangle edge makes the new nodal value to assume the average of the nodes in the edge.

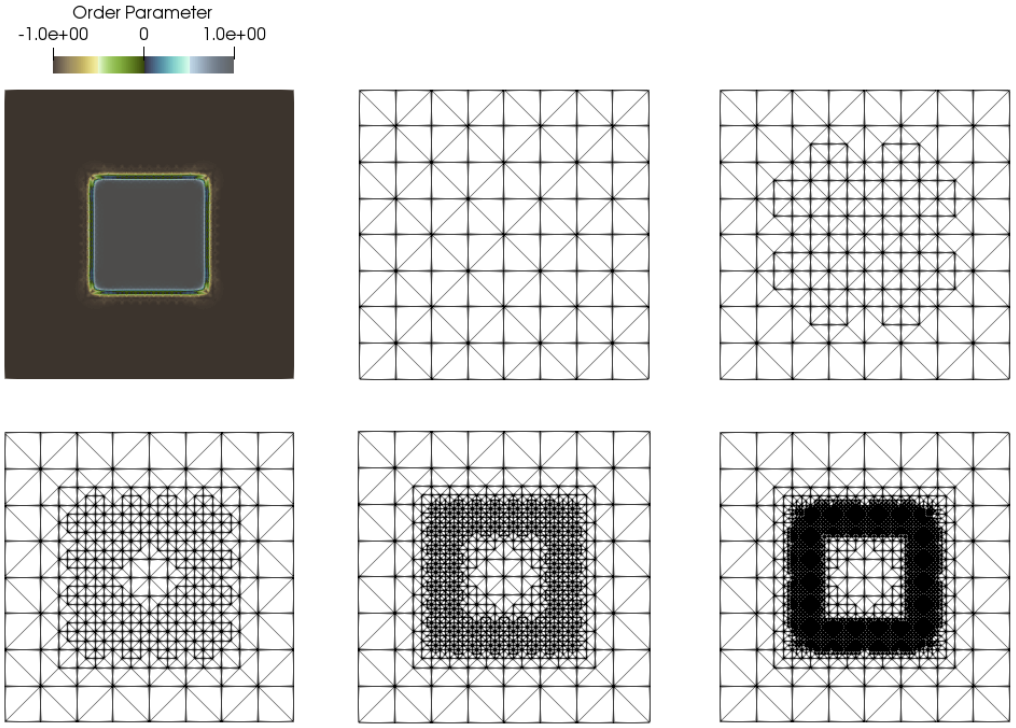

Figure 5.6: Iterative mesh refinement with four iterations. The error indicators track the local error on the previous fine mesh that surpasses the prescribed maximum norm of the mesh $||\eta||_\infty$ and the iterative mesh refinement procedure generates a mesh that preserves the maximum norm with less elements.

5.2.2 Numerical validation

To validate the spatial adaptivity scheme, we consider a constant mobility phase separation simulation. We considered the same initial conditions presented in Fig. 3.4 used for the simulation in section 3. The fixed mesh simulation presented in Section 3.6 consists of a triangular-element mesh with 129^2 nodes. To reach this same level of refinement during the adaptive procedure, a root mesh of 9^2 nodes is used and refined during four iterations, resulting in a mesh with equal refinement. In this section, to mark the elements to be refined, we consider the maximum norm of the error vector to be $||\eta||_\infty = 10^{-6}$ in both cases. As mentioned earlier, mesh discretization plays a major role in the Cahn-Hilliard modeling, since the interface domain must be well discretized to capture the thermodynamical transitions smoothly. Improper mesh discretizations interfere negatively on the interface motion and often generates unphysical results. That said, the space adaptivity must fulfill the prerequisite of representing the same physical results of the fixed mesh results. Figure 5.7 reveals the identical free energy decay in both cases, confirming that both results have the same level of accuracy but a different number of degrees of freedom. This is also seen on Figure 5.8 which shows the spinodal decomposition at the same time for both simulations.

Figure 5.9a shows that in the early stages of the adaptive simulation, the root mesh

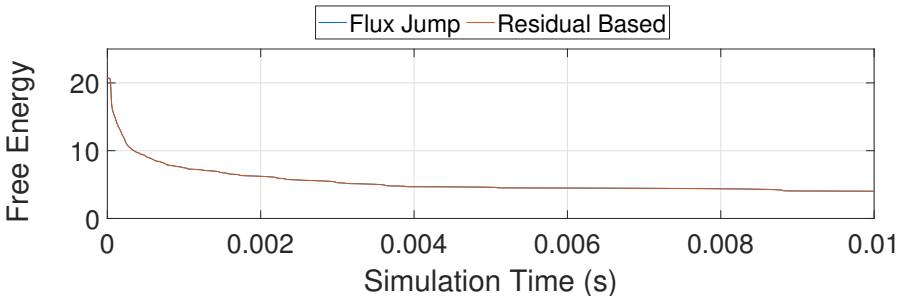

Figure 5.7: Free energy decay for both adaptive schemes

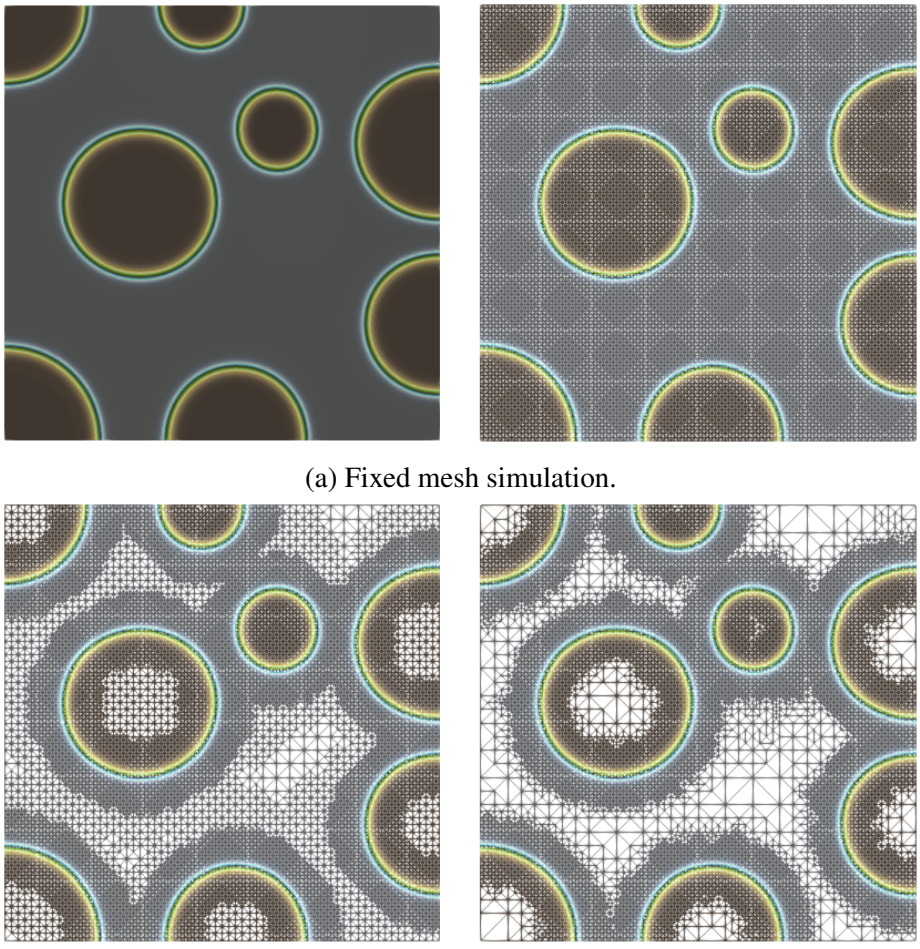

(a) Fixed mesh simulation.

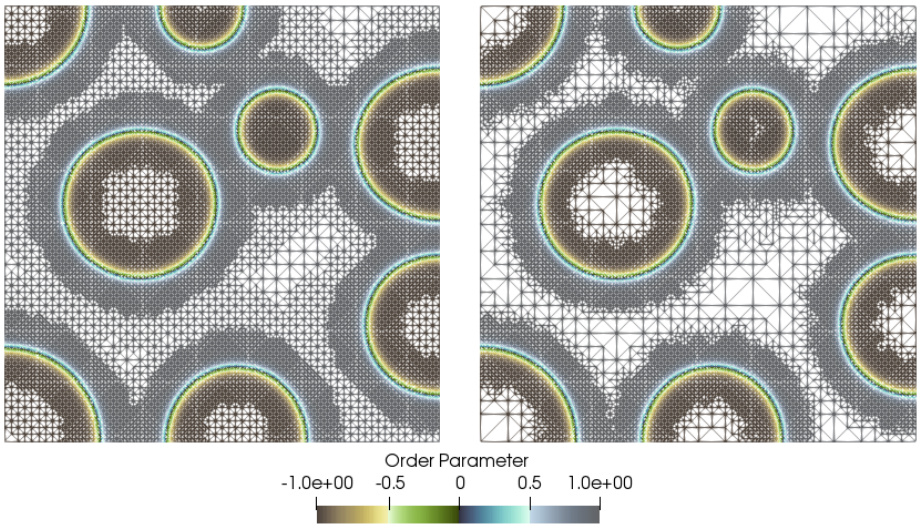

(b) Error indicator proposed by BAÑAS and NÜRNBERG [75] (left) and flux jump (right).

Figure 5.8: Solution of the spinodal decomposition at $t = 0.01s$. Two top figures are fixed mesh results. Bottom left figure represents the solution and mesh for the residual based error indicator and bottom right for the flux jump error indicator, revealing that at the same instant the physics that are being represented are the same.

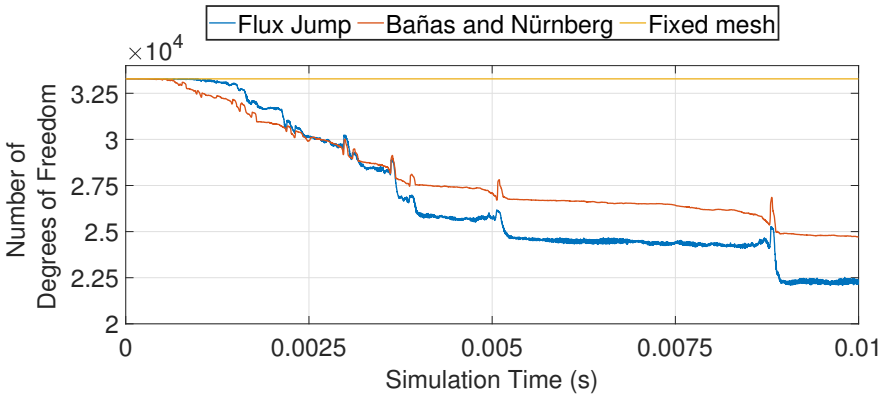

(a) Number of degrees of freedom for each simulation step

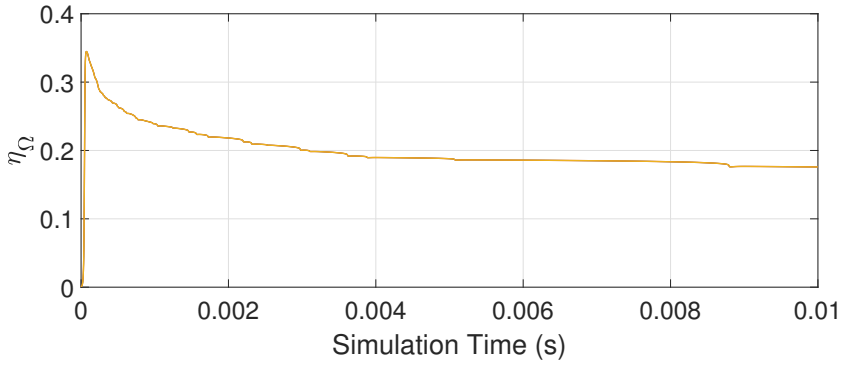

(b) Global error η_Ω for all three cases.

Figure 5.9: Variation of the number of degrees of freedom and the global spatial error η_Ω for both adaptive simulations with comparison to the fixed mesh simulation. The global error is preserved with reduced degrees of freedom.

Table 5.3: Comparison of the performance of both error indicators in relation to the fixed mesh simulation.

Error Indicator	Average Nonlinear System Size	Normalized CPU Time
Fixed Mesh	33282	1.000
Bañas and Nürnberg	28140	0.845
Flux Jump	27008	0.811

refined all of its elements, becoming a 129^2 node mesh until the interfaces became well defined. As soon as the bulk domain started to become larger, the error η_{el} of the bulk elements became lesser than the values defined as a refinement criterion. The satisfaction of this criterion is crucial to avoid the refinement on areas where the calculations are not important, providing a reduced nonlinear system. Such smaller errors occur thanks to the order of magnitude of the error at the bulk domains, which is significantly lesser than the errors found in the interface. As long as the simulation proceeds, the interfacial domain tends to shrink to a minimum, where the equilibrium takes place (steady-state). The constant reducing of the interfacial domain during the simulation reveals that the mesh refinement can significantly optimize the simulation without affecting the error. Figure 5.9b shows that the error is practically the same for both situations since the number of elements defining the interface is the same for both simulations. Nevertheless, Table 5.3 compares both error indicators, revealing that the flux jump revealed a smaller average nonlinear system in the simulations, presenting better overall performance on the tested case. At time $t = 0.01$s, it is clear that the reduced number of elements in the mesh produces the same error seen in the fixed mesh for both cases, showing that the fixed mesh is requiring unnecessary computational effort in the solution. However, if one aims to reduce the global error estimator η_Ω, a more refined root mesh or increased number of iterations would increase the number of elements representing the interface.

5.3 Space-time adaptivity

In this section, we combine both spatial and time adaptivity. Our objective is to take advantage of the spatial adaptivity scheme to reduce the number of degrees of freedom in our model by coarsening the mesh in the bulk domain while coupling the time adaptivity scheme to enlarge the time step size when possible. The union of these two schemes results in an optimal scheme to reduce the computational cost. We consider in the space-time adaptivity scheme the PC11 time step controller and the flux jump error indicator since both procedures presented the better results on their separate validations. Now, the section related to the time loop can be splitted into three parts - the spatial adaptivity procedure, the nonlinear system solver and the temporal adaptivity procedure - in this

sequence.

Note though that both adaptivity schemes are coupled, that is, both errors estimates interfere with each other [77]. During our simulations, we observed that calling the remeshing routine affects the temporal error directly since the solution vector obtained after the mesh adaptation procedure is solved in a different mesh while the other two past solutions have to be interpolated into the new mesh. Mesh adaptation procedures affect the length of the solution vectors at every time they are invoked. These solution vectors are used to estimate the temporal weighted local truncation error. Therefore, the interpolation procedure on `FEniCS` is called by a built-in function to bring the past two solution vectors needed to estimate the temporal error to the same length to the current solution vector. The `FEniCS` framework presents two different ways to interpolate the solution, the functions `interpolate` and `project`. The `interpolate` function is the same function used to interpolate the meshes on the iterative mesh refinement procedure described in section 5.2, where the new nodal values in the interpolated solution are obtained by the average of the nearest nodes. The solution is evaluated in the nodal coordinates $\mathbf{x}_{new}$ and averaged by their distances to the nearest nodes. That is, the new solution field $\tilde{\phi}$ is directly obtained by evaluating the solution ϕ on the coordinates $\mathbf{x}_{new}$. The `project` function consists on projecting the solution onto a new space of functions generated by the new mesh and evaluating the L^2-norm of both solutions by solving a linear system for the new nodal values, being often used for postprocessing ends such as turning discontinuous gradient fields into continuous ones or comparing higher- and lower-order function approximations [4]. The system to be solved is as follows: being V the space of functions in the new mesh, find $\tilde{\phi} \in V$ such that:

$$\int_\Omega \tilde{\phi} v d\Omega = \int_\Omega \phi v d\Omega \qquad \forall v \in V. \tag{5.20}$$

We tested both functions in our simulations, revealing identical results. In both cases, the new nodal values are not obtained from directly solving the equation, but evaluated from a previous solution on a different mesh. Thus, the interpolated solution now presents computational errors due to the approximation of the solution, being directly influenced by the prescribed tolerances of both adaptivity schemes. The time step controller evaluates these errors and consequently reduces the time step size, increasing the number of time steps evaluated. If the mesh refinement routine is set to be done at every time step, the errors become cumulative on every time step, increasing the temporal error r. Our investigation at this point is to verify if the use of the spatial adaptivity scheme coupled to time adaptivity improves the performance of the simulations even if the spatial adaptivity scheme leads to an increasing number of time steps. We observed that, if the maximum norm of the mesh $||\eta||_\infty$ is not strict enough, right after the mesh refinement routine is called, the time step size is instantly reduced to $O(10^{-9})$. Figure 5.10 and Table 5.4 com-

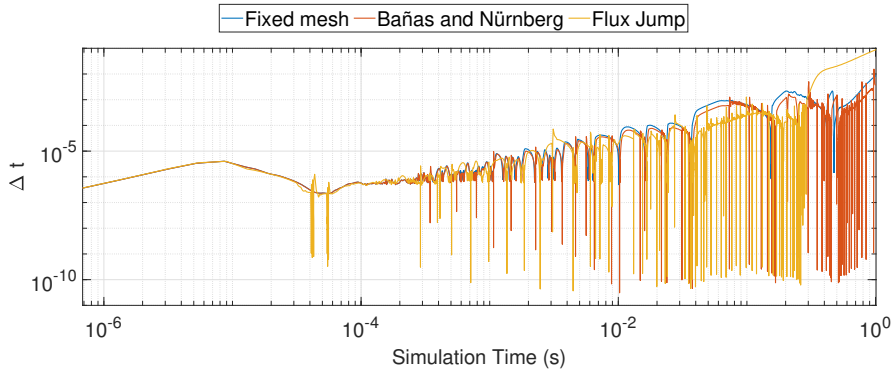

Figure 5.10: Time step behavior on both simulations with temporal adaptivity and space-time adaptivity schemes with $||\eta||_\infty = 10^{-4}$. Note that the time step is reduced everytime the refinement procedure is invoked. This effect compromise the performance of the simulations, since much more time steps are required to reach the steady-state.

Table 5.4: Performance of both spatial adaptivity schemes for the case of $||\eta||_\infty = 10^{-4}$.

Spatial Adaptivity Scheme	Time Steps	Average Nonlinear System Size	Normalized CPU Time
Fixed Mesh	4591	33282	1.000
Bañas and Nürnberg	9320	16361	0.998
Flux Jump	8882	16309	0.948

pare the performance of two space-time adaptivity schemes with prescribed values for $||\eta||_\infty$ for the spatial adaptivity strategy, revealing that in the situation where the $||\eta||_\infty$ is less strict, the performance improvement obtained from the temporal adaptivity scheme is compromised.

5.3.1 Numerical validation

Phase separation - constant mobility

After validating both spatial and temporal adaptivity schemes separately, we use the space-time adaptivity scheme in the same simulations to compare the accuracy of the methods. In this section we evaluate two different values for $||\eta||_\infty$ and we compare the performance of the simulation for the situations where the mesh is refined at every m time steps. For larger values of m, the simulations can lead to situations where the interface motion is captured by a coarsened region of the mesh, delaying the physics of the problem, leading to unphysical results. In some cases, when the mesh is too coarsened, the Newton solver can have convergence problems. When $||\eta||_\infty = 0$, all elements are refined at every iteration, becoming a fixed mesh simulation. We consider a root mesh of 9^2 nodes to be iteratively refined 4 times to reach elements with an equivalent size of a structured 129^2 nodes mesh in the interface domain. Figure 5.11 shows the steady-state

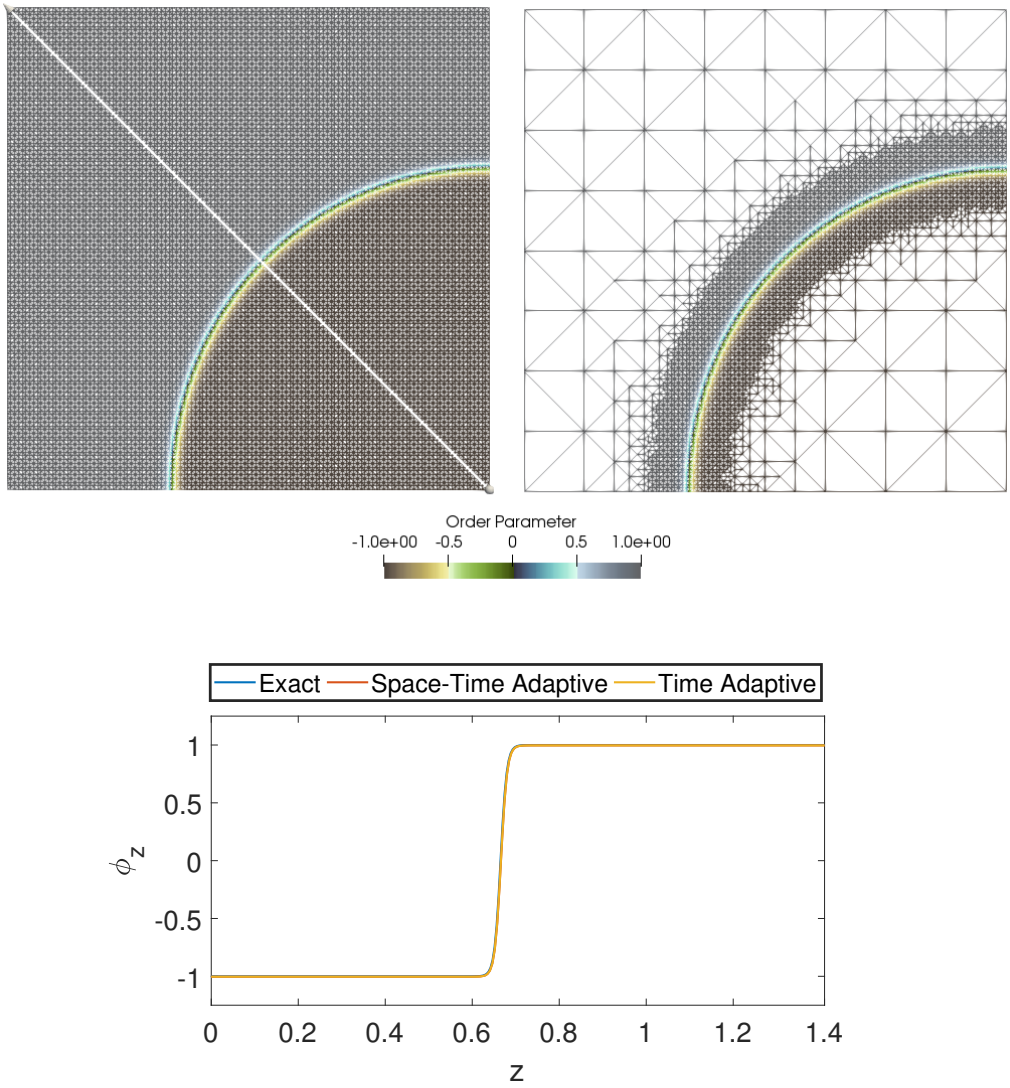

Figure 5.11: Assessment of the pure temporal and the space-time adaptive simulations in the steady-state. The equilibrium profile seen in Eq. (2.7) is compared with the numerical solution across a diagonal axis in the domain, revealing that the spatial discretization in both situations is fine enough to capture the interface.

of the Cahn-Hilliard equation after the space-time adaptivity scheme and the equilibrium concentration profile. The physics have the same dynamics in all cases, revealing that any adaptivity scheme used did not hamper the accuracy of the fixed mesh and time step simulations. This is also confirmed by Figure 5.12, since the reduction of the time step size is caused by the shrinkage of a given phase and occurs in every simulation in the same physical time thus revealing that the dynamics are preserved in every case.

Table 5.5 and Figures 5.12 and 5.13 compare the performance of the proposed simulations. When comparing the performance of the space-time adaptivity with the variable time step solutions with a fixed mesh, we note that the number of time steps calculated for the space-time scheme is larger than the pure time adaptive simulation, as well as the number of rejected time steps. This large number of time steps happens because after calling

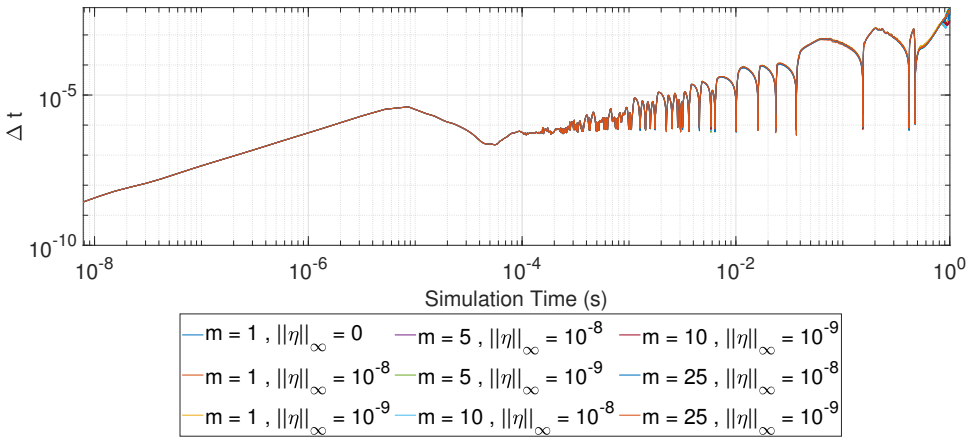

Figure 5.12: Time step behavior on the proposed simulations with space-time adaptivity schemes described on Table 5.5 presenting almost identical behavior.

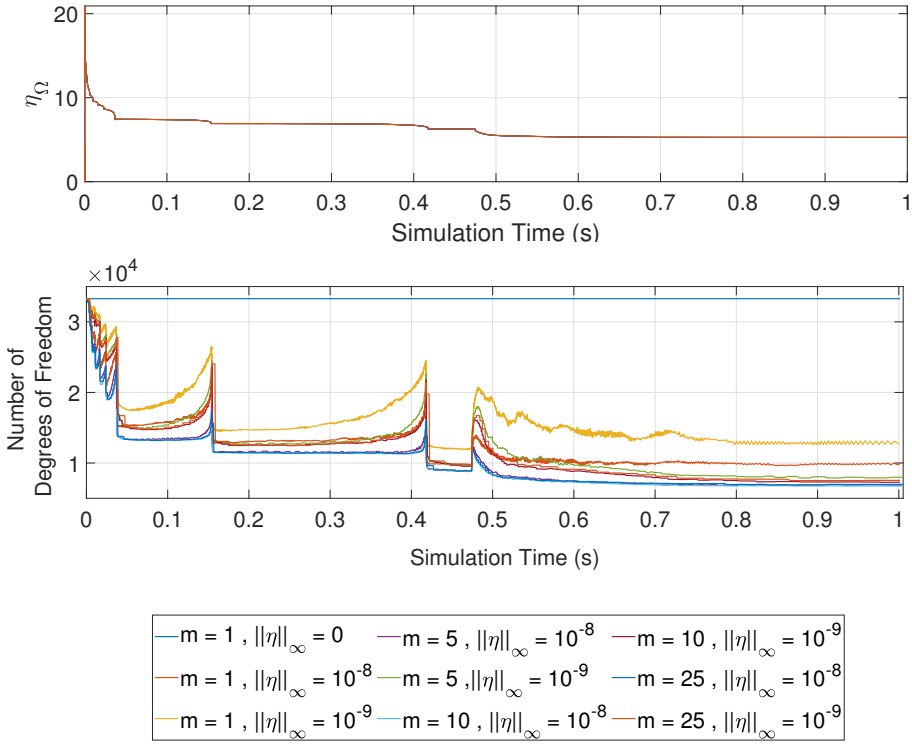

Figure 5.13: Global error η_Ω and number of degrees of freedom for each case presented on Table 5.5. The global error is almost identical for all cases while the adaptive schemes present less degrees of freedom.

Table 5.5: Comparison between the performance of the presented simulations.

$\|\|\eta\|\|_\infty$	m	Time Steps	Rejected Time Steps	Average Nonlinear System Size	Normalized CPU Time
0	1	4516	75	33282	1.0000
10^{-9}	1	4981	101	26379	0.8774
10^{-8}	1	5256	101	23346	0.8185
10^{-9}	5	5056	104	24642	0.8322
10^{-8}	5	5242	91	22003	0.7680
10^{-9}	10	5119	96	24014	0.8196
10^{-8}	10	5297	94	21598	0.7620
10^{-9}	25	5081	97	24317	0.8241
10^{-8}	25	5269	99	21793	0.7656

the mesh refinement procedure, the temporal error estimation possibly carries spatial error due to the mesh coarsening in the bulk domain, implying that the disturbance ζ described in Fig. 5.1 carries information about the physical, temporal error as well as the computational error generated by the mesh interpolation. However, this increased number of time steps evaluated is confronted with a significant reduction of the nonlinear system size in all cases. Comparing the average nonlinear system size on Table 5.5 with the presented results on Table 5.4, we note that the simulations presenting larger values of $||\eta||_\infty$ reveal smaller nonlinear systems during the simulation, at the cost of an increasing number of time steps evaluated. Evaluating the results, the best setup within the proposed simulations consist on refining the mesh at every 10 time steps and considering $||\eta||_\infty = 10^{-8}$. We consider these parameters for the simulations presented in the following examples.

Chapter 6

Numerical Applications

In this section, we extrapolate our methodology for different physical contexts where the Cahn-Hilliard equation can model. We consider a phase-separation with a degenerate mobility and a nonlocal Cahn-Hilliard equation which models the self-assembly of diblock copolymers.

6.1 Phase separation - degenerate mobility

Some applications involving the Cahn-Hilliard equation require the use of degenerate mobility, that is, a mobility coefficient which is a function of the concentration. This strategy increases the nonlinearity of the equation, increasing the computational effort of its solution. By using the degenerate mobility, the phases tend to have even slower dynamics, since the mobility is now restricted to the interfaces and not to the bulk domain. This strategy delays the Ostwald ripening phenomena, which can be unacceptable in certain physical contexts such as binary fluid flow, according to YUE *et al.* [78] and ABELS *et al.* [79].

In the phase separation context, using degenerate mobility also tends to slow the already slow dynamics of coarsening. That is, the steady-state reached under 1.0 second in the constant mobility setup now is expected to be reached within 10.0 to 20.0 seconds, making the use of time adaptivity schemes even more critical.

In this sense, we consider the following mobility parameter:

$$M(\phi) = \begin{cases} \bar{M}_0(1-\phi^2) & \text{if } -1 < \phi < 1, \\ 0 & \text{otherwise,} \end{cases} \tag{6.1}$$

where $\bar{M}_0 = 1$.

This simulation reaches the steady-state around 22.7 seconds of physical time. As expected, the dynamics of the Cahn-Hilliard equation for the degenerate mobility case is slower than the constant mobility in the mixture. The larger number of time steps required

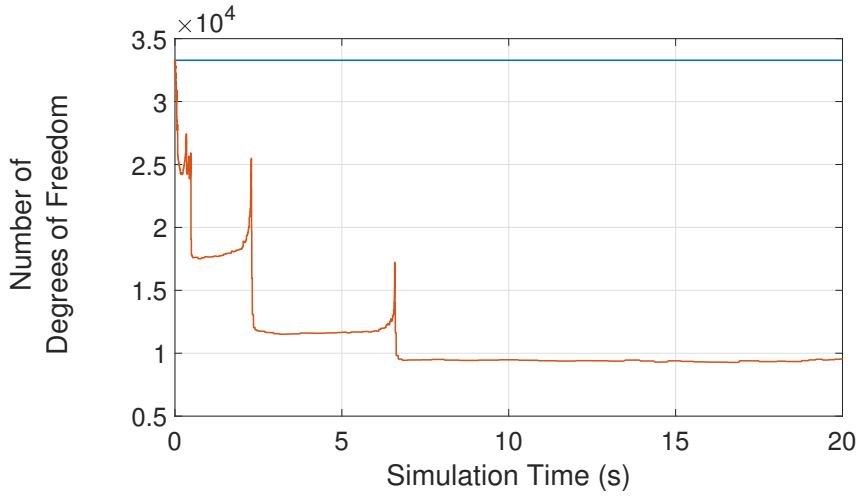

Figure 6.1: Comparison between the number of degrees of freedom in the pure temporal and space–time adaptive scheme. Reaching the steady-state presents much more computational cost when the mixture is modeled with degenerate mobility. The spatial adaptivity scheme reduces the size of the nonlinear systems to be solved significantly, while the temporal adaptive scheme can assume larger time steps thanks to the slower dynamics presented in this model.

Table 6.1: Comparison between space-time and time adaptivity schemes for the PC11 controller on degenerate mobility simulations. The last column takes into account both accepted and rejected steps.

Adaptivity Scheme	Time steps	Rejected steps	Nonlinear Systems Average Size	Normalized CPU Time
Time	5265	88	33282	1.0000
Space-Time	5303	84	26093	0.7890

to reach the steady-state in this scenario reinforces the use of adaptive time stepping. The use of constant $\Delta t = 2 \times 10^{-6}$s required to capture the fast dynamics in the phase separation sub-process would demand the calculation of 1.135×10^7 timesteps, instead of the usual $O(10^3)$ number of time steps obtained from the adaptive schemes as seen in Table 6.1. The Table compares the pure temporal and space-time adaptivity scheme, and the results are similar to the ones found in the constant mobility case. We can highlight the slightly smaller average size of the nonlinear system in the degenerate mobility case that can be explained by the slower dynamics, leading to even slower intermediate and advanced stages of phase separation. This slower stages usually have smaller interface domain, then yielding more coarsened meshes with improved efficiency, as seen in Fig. 6.1. Since the degenerate mobility model requires more time of simulated physics, it is desirable to use both adaptivity schemes to reach larger time step sizes using the pure temporal adaptivity scheme and to reduce the number of equations to be solved in the nonlinear system by using the spatial adaptivity scheme.

6.2 Diblock copolymer

The Cahn-Hilliard equation can be modified to model the self-assembly of copolymers (KIM *et al.* [14], CHOKSI *et al.* [28]). The order parameter ϕ is now the difference between the local volume fractions of two-component monomers. In this section, we consider the Ohta-Kawasaki model, where the Cahn-Hilliard equation is modified to:

$$\frac{\partial \phi}{\partial t} = \nabla \cdot \left[M(\phi) \nabla \left(\frac{\partial \Psi}{\partial \phi} - \epsilon^2 \nabla^2 \phi \right) \right] - \gamma(\phi - \bar{\phi}), \tag{6.2}$$

where γ is a nonlocal parameter related to the square of the total chain length of the polymer (OHNISHI *et al.* [80]) and $\text{mean}(\phi) = \bar{\phi} = \frac{1}{|\Omega|} \int_\Omega \phi d\Omega$ is the spatial average of ϕ. This extra reaction term reflects the first-order effects of the connectivity of the monomer chains, thus giving the nonlocal character to the equation (OHTA and KAWASAKI [27]).

In this section, we consider periodic boundaries and it is well known that this condition enables the Cahn-Hilliard mass conservation property. In this sense, the spatial average of ϕ is the same for all time steps, being part of the initial condition. Different from the pure Cahn-Hilliard equation that is derived from the Ginzburg-Landau functional, the modified Cahn-Hilliard equation presented on Eq. (6.2) is derived from a different free energy functional:

$$\begin{aligned} F[\phi] = \int_\Omega \left(\Psi(\phi) + \frac{\epsilon^2}{2} |\nabla \phi|^2 \right) d\Omega + \\ \frac{\gamma}{2} \int \int_\Omega G(\mathbf{x}, \mathbf{y}) (\phi(\mathbf{x}) - \bar{\phi})(\phi(\mathbf{y}) - \bar{\phi}) d\mathbf{x} d\mathbf{y}, \end{aligned} \tag{6.3}$$

where $G(\mathbf{x}, \mathbf{y})$ represents Green's function of $-\Delta$ on Ω with periodic boundary conditions.

In the diblock copolymer context, the free energy density function $\Psi(\phi)$ in the Eqs. (6.2) and (6.3) often are treated as the Flory-Huggins free energy density function, according to GHIASS *et al.* [81], which is:

$$\Psi(\phi) = \frac{k_B T}{v} \left[\frac{\phi}{l} \ln \phi + (1 - \phi) \ln(1 - \phi) + \chi \phi (1 - \phi) \right], \tag{6.4}$$

where v is the volume fraction of the element and l is the Kuhn statistical length, k_B is the Boltzmann constant, T is the absolute temperature and χ is the Flory-Huggins interaction parameter which measures the incompatibility of two monomers.

However, also according to GHIASS *et al.* [81], the parameters l and χ are often calibrated from experimental results and vary for different components. In this sense, it is possible to see the nonlocal Cahn-Hilliard equation from a different approach, where all these parameters can be expressed as a function of $\bar{\phi}$, γ and ϵ (CHOKSI *et al.* [28]). This

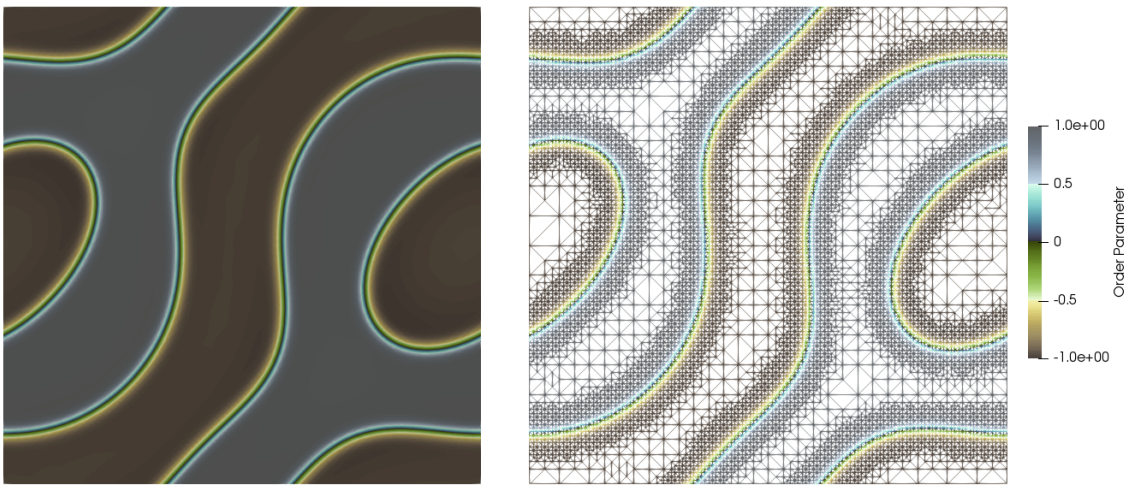

Figure 6.2: Nonlocal Cahn-Hilliard solution in the steady-state using the space-time adaptivity scheme. This example represents a 129^2 nodes mesh with $\lambda = 0.01$, $\gamma = 10^3$ and $\bar{\phi} = 0.0$.

Cahn-Hilliard setup can be seen as a mathematical paradigm for the modeling of periodic or quasi-periodic pattern formation induced by short-range and long-range interactions (SEUL and ANDELMAN [82]). This approach also allows the use of the conventional polynomial function of $\Psi(\phi)$ described by Eq. (2.3). Depending on the values of these three parameters, the minimization of the functional seen on Eq. (6.3) leads to different patterns between phases. We use the space-time adaptivity scheme presented in this study to reach the steady-state for each pattern more efficiently. Unlike all the other results presented in this study, we consider different initial conditions for each simulation in this section, since the parameter $\bar{\phi}$ is related to the mass conservation of the Cahn-Hilliard equation during all time steps and is one of the key parameters for the formation of different patterns. Also, we consider periodic boundary conditions in this section, to estimulate the development of the desired patterns. In this section, since the interfacial domain is much larger in the steady state than the previous examples, it is expected that the spatial adaptivity scheme presents smaller influence than in the previous cases. In this section, we evaluate different meshes and different values for $\epsilon^2 = \lambda$ to evaluate the relevance of these parameters into the spatial adaptivity scheme for the diblock copolymer scenario.

Initially we consider the same 129^2 nodes mesh used in the previous sections and $\lambda = 0.01$. Since we are considering periodic boundary conditions in this section, the mesh presents now a total of 32772 number of degrees of freedom. After numerical experiments, we observed that the spatial adaptivity scheme can be irrelevant for certain cases in the diblock copolymer context, not depending on $||\eta||_\infty$. For example, it can be seen in Fig. 6.2, a case with $\gamma = 10^5$ and $\bar{\phi} = 0.3$, that the interface domain in the steady-state of the nonlocal Cahn-Hilliard simulations is significantly larger than the other cases presented. This larger interface depends mostly on the nonlocal parameter γ and, in these situations, the spatial adaptivity does not add to the efficiency of the simulations.

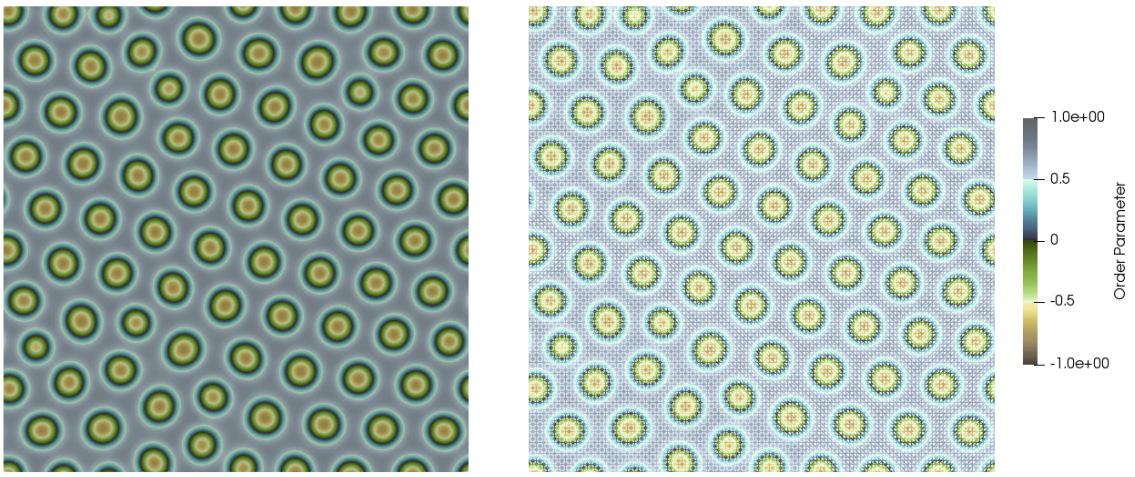

Figure 6.3: Nonlocal Cahn-Hilliard solution in the steady-state using the space-time adaptivity scheme. This example represents a 129^2 nodes mesh with $\lambda = 0.01$, $\gamma = 10^5$ and $\bar{\phi} = 0.3$.

However, if we consider situations where the nonlocal parameter has less significance in the model, we observe that the interfacial domain tends to diminish. We evaluate a situation within this context where $\gamma = 10^3$ and $\bar{\phi} = 0.0$, described in Fig. 6.3. In situations where the nonlocal parameter γ is significantly large, the entire domain tends to present interfacial values for the order parameter, implying on the non-existence of the bulk domain, meaning that all elements become flagged for refinement during the simulation. On situations where γ presents smaller orders of magnitude, the long-range interactions become weaker, and the spatial adaptivity scheme is now relevant for the simulations, even though the interfacial domain is still more representative than in the spinodal decomposition simulations. In all cases, we consider $||\eta||_\infty = 10^{-6}$, which is slightly larger than the prescribed value on the previous cases. However, the results presented on Table 6.3 reveals that the efficiency of the scheme is compromised for these parameters. The CPU time of the adaptive simulations indicates that the best scenario for the diblock copolymer simulation is when the mesh is not adaptive. When the spatial adaptivity scheme influences on the coupled scheme, the increasing number of time steps is not satisfactory.

To circumvent this situation, we consider an even finer discretization with smaller interface width to assess the performance of the spatial adaptivity scheme. We consider a 257^2 nodes mesh, with 131076 degrees of freedom and $\lambda = 0.005$. The interfacial thickness is thought to be related to the interfacial domain of the steady state in this situations. Thus we define these parameters to reduce the interfacial thickness, therefore increasing the bulk domain and allowing the use of different values for $||\eta||_\infty$. We consider the same two set of parameters described on Figs. 6.2 and 6.3. Since we altered the value for λ, we expected the pattern formation to change according to CHOKSI *et al.* [28]. The simulation presenting $\gamma = 10^5$ and $\bar{\phi} = 0.3$ presents the same pattern formation observed in the

Table 6.2: Performance of the space-time adaptivity scheme for each simulation of the nonlocal Cahn-Hilliard equation for a 129^2 nodes mesh and $\lambda = 0.01$. It can be observed that when the nonlocal parameter is strong enough, the interfacial domain is significant enough to not reduce the nonlinear system size. However, when the nonlocal parameter is weaker, the spatial adaptivity scheme can reduce the CPU time significantly, depending on the parameters and initial conditions.

Mesh	ϕ	γ	Average Nonlinear System Size	Time Steps	Normalized CPU Time
Fixed	0.0	10^5	32772	1061	1.0000
Adaptive	0.0	10^5	32772	1061	1.0000
Fixed	0.3	10^5	32772	689	1.0000
Adaptive	0.3	10^5	32772	689	1.0000
Fixed	0.0	10^3	32772	1453	1.0000
Adaptive	0.0	10^3	21188	2985	1.3282
Fixed	0.3	10^3	32772	2744	1.000
Adaptive	0.3	10^3	24789	6655	1.8147

Table 6.3: Performance of the space-time adaptivity scheme for each simulation of the nonlocal Cahn-Hilliard equation for a 257^2 nodes mesh with parameters $\gamma = 10^3$, $\bar{\phi} = 0.0$ and $\lambda = 0.005$. We consider a mesh refinement procedure at every 10 time steps.

$\|\|\eta\|\|_\infty$	Average Nonlinear System Size	Time Steps	Normalized CPU Time
0.0	131076	3186	1.0000
10^-6	68146	10547	1.7211
10^-7	86872	7308	1.5202
10^-8	129992	3753	1.1682

previous mesh and interface settings, described in Fig. 6.4. However, the situations where $\gamma = 10^3$ and $\phi = 0.0$ presented a different steady state from the previous section. In this sense, we evaluate the computational gain in this case, since the other set of parameters does not reveal any performance change for the spatial adaptivity scheme.

We note that the CPU time decreases with a finer mesh and smaller interface thickness even if the results are still not achieving proper CPU time for this case. However, we can observe that with even finer mesh discretization the coupled temporal-spatial adaptivity scheme can be able to improve the simulation of this type of physical phenomenon.

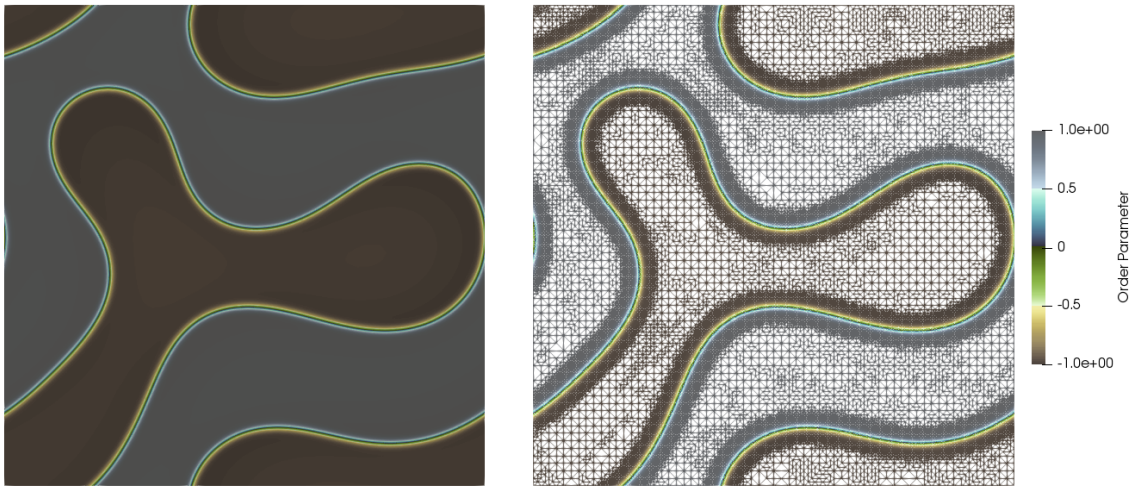

Figure 6.4: Nonlocal Cahn-Hilliard solution in the steady-state using the space-time adaptivity scheme. This example represents a 129^2 nodes mesh with $\lambda = 0.01$, $\gamma = 10^5$ and $\bar{\phi} = 0.3$.

Chapter 7

Conclusions and future works

7.1 Conclusions

In this study, we propose an adaptive scheme for the Cahn-Hilliard equation and evaluate its performance on different physical contexts. Initially we evaluate each scheme separately. For the spatial adaptivity scheme, we consider two error indicators coupled with the bissection method for refinement. After some numerical simulations, the flux jump presented better results and was carried to the space-time adaptivity scheme. For the temporal adaptivity scheme, we considered the linear feedback control theory to design a proper time step size to keep the estimated temporal error within the prescribed tolerances. We evaluated three controllers, where the PC11 presents better results, and an error estimation procedure which does not require the necessity of the calculation of the same step twice or three times. For the space-time scheme, we observe that when coupling both adaptivity schemes, the interplay between the prescribed tolerances for each case interfere directly on the performance of the simulations. For larger values of the allowed maximum norm $||\eta||_\infty$, the mesh becomes more coarsened, but the spatial error is captured by the temporal estimator. If the maximum norm is tighter, the mesh becomes less coarsened, not improving on the reduction of the nonlinear system. The evaluation of this interplay is fundamental to validate the coupled adaptivity scheme. We concluded that for this coupling, the refinement being called at every 10 time steps and the maximum prescribed norm of $||\eta||_\infty = 10^{-8}$ is the optimum setup.

When analyzing each adaptivity scheme individually, we conclude that the temporal adaptivity scheme is much more efficient than the spatial adaptivity scheme in comparison to both fixed mesh and fixed time step simulations. When comparing spinodal decomposition simulations from the unstable mixture until the complete phase separation, the temporal adaptivity scheme, when submitted to proper prescribed tolerances, can present a ratio of solved time steps of $1/1000$, that is, one adaptive time step is solved at every 1000 fixed time steps.

We extended this setup to examples such as spinodal decomposition with constant and nonlinear mobilities and diblock copolymer self-assembly using the nonlocal Cahn-Hilliard equation. For the spinodal decomposition example, we reach good performance with our set of parameters while for the nonlocal Cahn-Hilliard equation, due to the significant presence of interfacial domain, the scheme becomes better as the interfaces become thinner.

7.2 Future works

Our suggestion for future related works:

- Extension for 3D simulations, which presents more complex phenomena and reaches different steady-state patterns for the nonlocal Cahn-Hilliard equation;
- Nonlocal Cahn-Hilliard simulations with smaller values of λ and finer meshes to increase the bulk domain and eventually reach a CPU time lesser than 1.00;
- Implementation of different NSCH models (described on Table 4.1);
- Proper tuning of the parameters κ_P, κ_I and κ_D to reach optimum performance;
- Spatial adaptivity scheme using anisotropic refinement to optimize the mesh size reduction.

References

[1] QIN, R. S., BHADESHIA, H. K. "Phase field method", *Materials Science and Technology*, v. 26, n. 7, pp. 803–811, 2010.

[2] PROVATAS, N., ELDER, K. *Phase-Field Methods in Material Science and Engineering*. Wiley-VCH, 2010.

[3] ZIENKIEWICZ, O. C., TAYLOR, R. L. *The Finite Element Method Volume 1: The Basis*. Butterworth-Heinemann, 2000.

[4] LOGG, A., MARDAL, K. A., WELLS, G. N., et al. *Automated Solution of Differential Equations by the Finite Element Method*. Springer, 2012.

[5] SÖDERLIND, G. "Digital filters in adaptive time-stepping", *ACM Transactions on Mathematical Software*, v. 29, n. 1, pp. 1–26, 2003.

[6] BAZILEVS, Y., TAKIZAWA, K., TEZDUYAR, T. E. *Computational Fluid-Structure Interaction: Methods and Applications*. 2012.

[7] DONEA, J., HUERTA, A. *Finite Element Methods for Flow Problems*. John Wiley & Sons, Ltd., 2003.

[8] FRIEDMAN, A. "Free Boundary Problems in Science and Technology". v. 47, pp. 854–861. Notices of the AMS, 2000.

[9] CHEN, G. Q., SHAHGHOLIAN, H., VAZQUEZ, J. "Free Boundary Problems: The Forefront of Current and Future Developments", *Philosophical transactions. Series A, Mathematical, physical, and engineering sciences*, v. 373, n. 2050, 2015.

[10] GOMEZ, H., VAN DER ZEE, K. G. "Computational Phase-Field Modeling", *Encyclopedia of Computational Mechanics Second Edition*, 2017.

[11] HAATAJA, M., MAHON, J., PROVATAS, N., et al. "Scaling of domain size during spinodal decomposition: Dislocation discreteness and mobility effects", *Applied Physics Letters*, v. 87, pp. 87–89, 2005.

[12] COLEMAN, B. D., NOLL, W. "The thermodynamics of elastic materials with heat conduction and viscosity", *Archive for Rational Mechanics and Analysis*, v. 13, n. 1, pp. 167 – 178, 1963.

[13] CAGINALP, G. "Stefan and Hele-Shaw type models as asymptotic limits of the phase-field equations", *Phys. Rev. A*, v. 39, n. 11, pp. 5887–5896, 1989.

[14] KIM, J., LEE, S., CHOI, Y., et al. "Basic Principles and Practical Applications of the Cahn-Hilliard Equation", *Mathematical Problems in Engineering*, v. 2016, n. ID 9532608, pp. 11, 2016.

[15] BIBEN, T. "Phase-field models for free-boundary problems", *European Journal of Physics*, v. 26, n. 5, 2005.

[16] CAHN, J. W., HILLIARD, J. E. "Free energy of a nonuniform system. I. Interfacial free energy", *The Journal of Chemical Physics*, v. 28, n. 2, pp. 258–267, 1958.

[17] VIGNAL, P., COLLIER, N., DALCIN, L., et al. "An energy-stable time-integrator for phase-field models", *Computer Methods in Applied Mechanics and Engineering*, v. 316, pp. 1179–1214, 2017.

[18] LEE, D., HUH, J. Y., JEONG, D., et al. "Physical, mathematical, and numerical derivations of the Cahn-Hilliard equation", *Computational Materials Science*, v. 81, pp. 216–225, 2014.

[19] LANDAU, L. D., LIFSHITZ, E. M. *Statistical Physics*. 1960.

[20] CAHN, J. W. "On spinodal decomposition", *Acta Metallurgica*, v. 9, n. 9, pp. 795–801, 1961.

[21] COPETTI, M. I. M., ELLIOTT, C. M. "Numerical analyisis of a Cahn-Hilliard equation with a logarithmic free energy", *Numerische Mathematik*, v. 63, n. 1, pp. 39–65, 1992.

[22] BINER, S. B. "An Overview of the Phase-Field Method and Its Formalisms". In: *Programming Phase-Field Modeling*, Springer International Publishing, pp. 1–7, 2017.

[23] BADALASSI, V. E., CENICEROS, H. D., BANERJEE, S. "Computation of multiphase systems with phase field models", *Journal of Computational Physics*, v. 190, n. 2, pp. 371–397, 2003.

[24] ROWLINSON, J. S. "Translation of J. D. van der Waals' "The thermodynamik theory of capillarity under the hypothesis of a continuous variation of density"", *Journal of Statistical Physics*, v. 20, n. 2, pp. 197–200, 1979.

[25] BRAY, A. J. "Theory of phase ordering kinetics", *Physica A: Statistical Mechanics and its Applications*, v. 194, n. 1-4, pp. 41–52, 1995.

[26] CAHN, J. W. "Free energy of a nonuniform system. II. Thermodynamic basis", *The Journal of Chemical Physics*, v. 30, n. 5, pp. 1121–1124, 1959.

[27] OHTA, T., KAWASAKI, K. "Equilibrium Morfology of Block Copolymer Melts", *Macromolecules*, v. 19, n. 10, pp. 2621–2632, 1986.

[28] CHOKSI, R., PELETIER, M. A., WILLIAMS, J. F. "On the Phase Diagram for Microphase Separation of Diblock Copolymers: An Approach via a Nonlocal Cahn-Hilliard Functional", *SIAM Journal on Applied Mathematics*, v. 69, n. 6, pp. 1712–1738, 2009.

[29] BERTOZZI, A. L., ESEDOGLU, S., GILLETTE, A. "Inpainting of binary images using the Cahn-Hilliard equation", *IEEE Transactions on Image Processing*, v. 16, n. 1, pp. 285–291, 2007.

[30] BORDEN, M. J., CLEMENS, V. V., SCOTT, M. A., et al. "A phase-field description of dynamic brittle fracture." *Computer Methods in Applied Mechanics and Engineering*, v. 217, pp. 77–95, 2012.

[31] SILVA JR, M. N., DUDA, F. P., FRIED, E. "Sharp-crack limit of a phase-field model for brittle fracture", *Journal of the Mechanics and Physics of Solids*, v. 61, n. 11, pp. 2178–2195, 2013.

[32] WU, X., VAN ZWIETEN, G. J., VAN DER ZEE, K. G. "Stabilized second-order convex splitting schemes for Cahn-Hilliard models with application to diffuse-interface tumor-growth models", *International Journal for Numerical Methods in Biomedical Engineering*, v. 30, n. 2, pp. 180–203, 2013.

[33] WISE, S. M., LOWENGRUB, J. S., CRISTINI, V. "An adaptive multigrid algorithm for simulating solid tumor growth using mixture models", *Mathematical and Computer Modelling*, v. 53, n. 1-2, pp. 1–20, 2011.

[34] ZHOU, S., WANG, M. Y. "Multimaterial structural topology optimization with a generalized Cahn-Hilliard model of multiphase transition", *Structural and Multidisciplinary Optimization*, v. 33, pp. 89–111, 2006.

[35] ELLIOTT, C. M., SONGMU, Z. "On the Cahn-Hilliard equation", *Archive for Rational Mechanics and Analysis*, v. 96, n. 4, pp. 339–357, 1986.

[36] EYRE, D. J. "Unconditionally Gradient Stable Time Marching the Cahn-Hilliard Equation", *MRS Proceedings*, v. 529, n. 39, 1998.

[37] STOGNER, R. H., CAREY, G. F., MURRAY, B. T. "Approximation of Cahn-Hilliard diffuse interface models using parallel adaptive mesh refinement and coarsening with C^1 elements", *International Journal for Numerical Methods in Engineering*, v. 76, n. 5, pp. 636–661, 2008.

[38] GOMEZ, H., CALO, V., BAZILEVS, Y., et al. "Isogeometric analysis of the Cahn–Hilliard phase-field model", *Computer Methods in Applied Mechanics and Engineering*, v. 197, n. 49-50, pp. 4333–4352, 2008.

[39] WELLS, G. N., KUHL, E., K., G. "A discontinuous Galerkin method for the Cahn-Hilliard equation", *Journal of Computational Physics*, v. 218, n. 2, pp. 860–877, 2006.

[40] ELLIOT, C. M., FRENCH, D. A., MILNER, F. A. "A second order splitting method for the Cahn-Hilliard equation", *Numerische Mathematik*, v. 54, n. 5, pp. 575–590, 1989.

[41] VAN DER ZEE, K. G., ODEN, J. T., PRUDHOMME, S., et al. "Goal-oriented error estimation for Cahn-Hilliard models of binary phase transition", *Numerical Methods for Partial Differential Equations*, v. 27, n. 1, pp. 160–196, 2010.

[42] ELLIOTT, C. M., STUART, A. M. "The global dynamics of discrete semilinear parabolic equations", *SIAM Journal on Numerical Analysis*, v. 30, n. 6, pp. 1622–1663, 1993.

[43] SHEN, J. "Modeling and numerical approximation of two-phase incompressible flows by a phase-field approach", *Multiscale Modeling and Analysis for Materials Simulation*, pp. 147–195, 2012.

[44] KELLEY, C. T. *Iterative methods for linear and nonlinear equations*. SIAM, 1995.

[45] WODO, O., GANAPATHYSUBRAMANIAN, B. "Computationally efficient solution to the Cahn-Hilliard equation: Adaptive implicit time schemes, mesh sensitivity analysis and the 3D isoperimetric problem", *Journal of Computational Physics*, v. 230, n. 15, pp. 6037–6060, 2011.

[46] ALNÆS, M. S., BLECHTA, J., HAKE, J., et al. "The FEniCS Project Version 1.5", *Archive of Numerical Software*, v. 3, n. 100, 2015.

[47] BALAY, S., GROPP, W. D., MCINNES, L. C., et al. "Efficient Management of Parallelism in Object Oriented Numerical Software Libraries". In: Arge, E., Bruaset, A. M., Langtangen, H. P. (Eds.), *Modern Software Tools in Scientific Computing*, pp. 163–202. Birkhäuser Press, 1997.

[48] HEROUX, M. A., BARTLETT, R. A., HOWLE, V. E., et al. "An overview of the Trilinos project", *ACM Trans. Math. Softw.*, v. 31, n. 3, pp. 397–423, 2005.

[49] VASCONCELOS, D. F., ROSSA, A. L., COUTINHO, A. L. "A residual-based Allen-Cahn phase field model for the mixture of incompressible fluid flows", *International Journal for Numerical Methods in Fluids*, v. 75, n. 9, pp. 645–667, 2014.

[50] GURTIN, M. E., POLIGNONE, D., VINALS, J. "Two-phase binary fluids and immiscible fluids described by an order parameter", *Mathematical Models and Methods in Applied Sciences*, v. 06, n. 06, pp. 815–831, 1996.

[51] HOHENBERG, P., HALPERIN, B. "Theory of dynamic critical phenomena", *Reviews of Modern Physics*, v. 49, n. 3, pp. 436–479, 1977.

[52] HOSSEINI, B. S., TUREK, S., MÖLLER, M., et al. "Isogeometric Analysis of the Navier–Stokes–Cahn–Hilliard equations with application to incompressible two-phase flows", *Journal of Computational Physics*, v. 348, pp. 171–194, 2017.

[53] LOWENGRUB, J., TRUSKINOVSKY, L. "Quasi-incompressible Cahn-Hilliard fluids and topological transitions", *Proceedings of the Royal Society A: Mathematical, Physical and Engineering Sciences*, v. 454, n. 1978, pp. 2617–2654, 1998.

[54] DING, H., SPELT, P., C., S. "Diffuse interface model for incompressible two-phase flows with large density ratios", *Journal of Computational Physics*, v. 226, n. 2, pp. 2078–2095, 2017.

[55] BOYER, F. "A theoretical and numerical model for the study of incompressible mixture flows", *Computers and Fluids*, v. 31, n. 1, pp. 41–68, 2002.

[56] SHEN, J., YANG, X. "A Phase-Field Model and Its Numerical Approximation for Two-Phase Incompressible Flows with Different Densities and Viscosities", *SIAM Journal on Scientific Computing*, v. 32, n. 3, pp. 1159–1179, 2010.

[57] ABELS, H., GARCKE, H., GRÜN, G. "Thermodynamically consistent, frame indifferent diffuse interface models for incompressible two-phase flows with different densities", *Mathematical Models and Methods in Applied Sciences*, v. 22, n. 3, pp. 1–40, 2012.

[58] SHEN, J., XIAOFENG, Y. "Decoupled, energy stable schemes for phase-field models of two-phase incompressible flows", *SIAM Journal of Numerical Analysis*, v. 53, n. 1, pp. 279–296, 2015.

[59] TAYLOR, C., HOOD, P. "A Numerical Solution of the Navier-Stokes Equations Using Finite Element Technique", *Computers and Fluids*, v. 1, n. 1, pp. 73–100, 1973.

[60] JOSHI, V., JAIMAN, R. K. "A positivity preserving variational method for multi-dimensional convection–diffusion–reaction equation", *Journal of Computational Physics*, v. 339, pp. 247–284, 2017.

[61] BROOKS, A. N., HUGHES, T. J. "Streamline upwind/Petrov-Galerkin formulations for convection dominated flows with particular emphasis on the incompressible Navier-Stokes equations", *Computer Methods in Applied Mechanics and Engineering*, v. 32, n. 1-3, pp. 199–259, 1982.

[62] HUGHES, T. J. R., FRANCA, L. P., HULBERT, G. M. "A new finite element formulation for computational fluid dynamics: VIII. The galerkin/least-squares method for advective-diffusive equations", *Computer Methods in Applied Mechanics and Engineering*, v. 73, n. 2, pp. 173–189, 1989.

[63] HUGHES, T. J. R. "Multiscale phenomena: Green's functions, the Dirichlet-to-Neumann formulation, subgrid scale models, bubbles and the origins of stabilized methods", *Computer Methods in Applied Mechanics and Engineering*, v. 127, n. 1-4, pp. 387–401, 1995.

[64] CHORIN, A. "Numerical Solution of the Navier-Stokes EquationsI)", *Mathematics of Computation*, v. 22, pp. 745–762, 1968.

[65] TEMAM, R. "Sur l'approximation de la solution des équations de Navier-Stokes par la méthode des pas fractionnaires (II)", *Archive for Rational Mechanics and Analysis*, v. 33, pp. 377–385, 1969.

[66] GUILLÉN-GONZÁLEZ, F., TIERRA, G. "Second order schemes and time-step adaptivity for Allen-Cahn and Cahn-Hilliard models", *Computers and Mathematics with Applications*, v. 68, n. 8, pp. 821–846, 2014.

[67] ZHANG, Z., QIAO, Z. "An adaptive time-stepping strategy for the Cahn-Hilliard equation", *Communications in Computational Physics*, v. 11, n. 4, pp. 1261–1278, 2012.

[68] CUETO-FELGUEROSO, L., PERAIRE, J. "A time-adaptive finite volume method for the Cahn-Hilliard and Kuramoto-Sivashinsky equations", *Journal of Computational Physics*, v. 227, n. 24, pp. 9985–10017, 2008.

[69] SÖDERLIND, G. "Time-step selection algorithms: Adaptivity, control, and signal processing", *Applied Numerical Mathematics*, v. 56, n. 3-4, pp. 488–502, 2006.

[70] SÖDERLIND, G. "Automatic control and adaptive time-stepping", *Numerical Algorithms*, v. 31, n. 1-4, pp. 281–310, 2002.

[71] VALLI, A. M. P., CAREY, G. F., COUTINHO, A. L. G. A. "Control strategies for timestep selection in finite element simulation of incompressible flows and coupled reaction-convection-diffusion processes", *International Journal for Numerical Methods in Fluids*, v. 47, n. 3, pp. 201–231, 2005.

[72] AHMED, N., JOHN, V. "Adaptive time step control for higher order variational time discretizations applied to convection-diffusion-reaction equations", *Computer Methods in Applied Mechanics and Engineering*, v. 285, pp. 83–101, 2015.

[73] CENICEROS, H. D., ROMA, A. M. "A nonstiff, adaptive mesh refinement-based method for the Cahn-Hilliard equation", *Journal of Computational Physics*, v. 225, n. 2, pp. 1849–1862, 2007.

[74] CAREY, G. F. *Computational Grids: Generation, Adaptation, and Solution Strategies*. Taylor Francis, 1997.

[75] BAÑAS, L., NÜRNBERG, R. "Adaptive finite element methods for Cahn-Hilliard equations", *Journal of Computational and Applied Mathematics*, v. 218, n. 1, pp. 2–11, 1984.

[76] RIVARA, M. C. "Mesh refinement processes based on the generalized bisection of simplices", *SIAM Journal on Numerical Analysis*, v. 21, n. 3, pp. 604–613, 1984.

[77] ILIE, S., SÖDERLIND, G., CORLESS, R. M. "Adaptivity and computational complexity in the numerical solution of ODEs", *Journal of Complexity*, v. 24, n. 3, pp. 341–361, 2008.

[78] YUE, P., ZHOU, C., FENG, J. J. "Spontaneous shrinkage of drops and mass conservation in phase-field simulations", *Journal of Computational Physics*, v. 223, n. 1, pp. 1–9, 2007.

[79] ABELS, H., DEPNER, D., GARCKE, H. "On an incompressible Navier-Stokes/Cahn-Hilliard system with degenerate mobility", *Annales de l'Institut Henri Poincare (C) Analyse Non Lineaire*, v. 30, n. 6, pp. 1175–1190, 2013.

[80] OHNISHI, I., NISHIURA, Y., IMAI, M., et al. “Analytical solutions describing the phase separation driven by a free energy functional containing a long-range interaction term”, *Chaos*, v. 9, n. 2, pp. 329–341, 1999.

[81] GHIASS, M., MOGHBELI, M. R., ESFANDIAN, H. “Numerical Simulation of Phase Separation Kinetic of Polymer Solutions Using the Spectral Discrete Cosine Transform Method”, *Journal of Macromolecular Science, Part B: Physics*, v. 55, n. 4, pp. 411–425, 2016.

[82] SEUL, M., ANDELMAN, D. “Domain shapes and patterns: The phenomenology of modulated phases”, *Science*, v. 267, n. 5197, pp. 476–483, 1995.

Appendix A

CDR Stabilization

Consider the general convection-diffusion-reaction equation given on eq. A.1. Since time integration is dealt independently from spatial integration, its steady state (eq. A.2) is considered.

$$\frac{\partial \phi}{\partial t} + \mathbf{u} \cdot \nabla \phi - \nabla \cdot (\mathbf{k} \nabla \phi) + s\phi = f, \tag{A.1}$$

$$\mathbf{u} \cdot \nabla \phi - \nabla \cdot (\mathbf{k} \nabla \phi) + s\phi = f, \tag{A.2}$$

where $\mathbf{u}$ is the convection velocity, $\mathbf{k}$ is the diffusivity tensor, s is the reaction term and ϕ the quantity transported. The convection-diffusion-reaction problems can be parametrized by non-dimensional numbers. The Peclet number (Pe) represents the significance of convection relative to diffusion. For large Pe, convection dominates, while for small Pe diffusion dominates. The convection-dominant case gives rise to interior and boundary layers in ϕ, which causes difficulties in the numerical approximation of the convection-diffusion-reaction equation. Diffusion-dominant cases reveal good approximation within the Galerkin framework (DONEA and HUERTA [7]). Figure A.1 shows different Pe solutions for the CDR equation: a one dimension domain is assumed, advective velocity is constant and points from left to right, and ϕ is set to unity on the left side of the interval and zero on the right side. For $Pe = 0$ the analytic solution is a straight line connecting the prescribed boundary values. As the Pe number increases, the solution forms a thin boundary layer on the right side of the domain. Solutions containing large gradients present a source of difficulty for numerical approximation of the convection–diffusion-reaction equation.

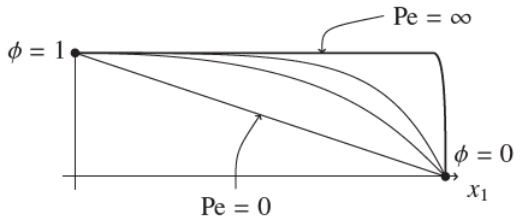

Figure A.1: Illustration of the solution behavior for the Convection–diffusion equation at Pe number ranging from zero to nearly infinity. From BAZILEVS [6].

Another important non-dimensional number is the Damköhler number (Da), which represents the significance of reaction relative to convection. The Damköhler number is widely used in chemical engineering to relate the chemical reaction timescale (reaction rate) to the transport phenomena rate occurring in a system. For large Da reaction dominates, while for small Da convection dominates. The case $Da = \infty$ corresponds to pure reaction, meaning that the whole substance was converted during transport.

In order to numerically solve the convection-diffusion-reaction equation using the finite element method, we need to introduce the variational form and spatial discretization. The discretization of the spatial domain Ω into nel number of elements is such that $\Omega = \cup_{e=1}^{nel} \Omega^e$ and $\emptyset = \cap_{e=1}^{nel} \Omega^e$. Considering S^h the space of the test functions and V^h the space of the weight functions, the weak (variational) formulation of the CDR equation becomes: find $\phi^h(\mathbf{x}) \in S^h$ such that $\forall w^h \in V^h$:

$$\int_\Omega \big(w^h(\mathbf{u}\cdot\nabla\phi^h) + w^h\nabla\cdot(\mathbf{k}\nabla\phi^h) + w^h s\phi^h)\big)d\Omega = \int_\Omega w^h f d\Omega \qquad \forall w^h \in V^h. \quad \text{(A.3)}$$

Using the divergence theorem and the fact that $w^h = 0$ on Γ_D, eq. (A.4) becomes:

$$\int_\Omega \big(w^h(\mathbf{u}\cdot\nabla\phi^h) + \nabla w^h\cdot(\mathbf{k}\nabla\phi^h) + w^h s\phi^h)\big)d\Omega = \\ = \int_\Omega w^h f d\Omega + \int_{\Gamma_N} w^h g d\Gamma \quad \forall w^h \in V^h. \qquad \text{(A.4)}$$

As said on chapter **??**, the Galerkin method essentially means that the function spaces V^h and S^h are the same (for trial functions and weight functions). However, when dealing with some situations (a convection dominated convection-diffusion equation, for example), the standard Galerkin method becomes unstable and prone to spurious global oscillations. The Petrov-Galerkin approach solves this problem by changing the space of the weight functions (that means the $w^h \notin V^h$). For example, considering one dimentional linear elements, the Streamline-Upwind Petrov-Galerkin (SUPG) method weight function now becomes:

$$\widetilde{w}^h = w^h + \alpha p, \qquad \text{(A.5)}$$

where p is such that $\int_L p dx = \pm\frac{h}{2}$, being h the element size. This means that the Petrov-Galerkin weight function is now the Galerkin weight function added to its derivative (multiplied by a scalar α, proportional to $\mathbf{u}$). Figure A.2 shows an example of a 1D linear SUPG weight function.

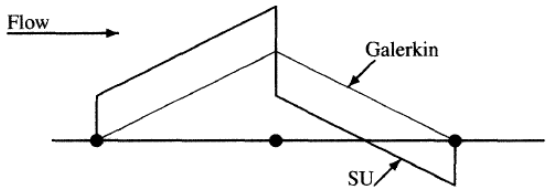

Figure A.2: Weighting function of the Streamline-Upwind Petrov-Galerkin (SUPG) method for linear elements. From DONEA and HUERTA [7].

However, since the weight functions are now discontinuous, the divergence theorem can be problematic. To avoid that, it can be considered that the Petrov-Galerkin weighting is continuous only in the interior of the finite elements. In that case, the SUPG formulation becomes:

$$\begin{aligned}
&\int_\Omega \big(w^h(\mathbf{u}\cdot\nabla\phi^h) + \nabla w^h\cdot(\mathbf{k}\nabla\phi^h) + w^h s\phi^h\big)d\Omega + \\
&+\sum_{e=1}^{nel}\int_\Omega \mathbf{u}\cdot\nabla w^h \tau(\mathbf{u}\cdot\nabla\phi^h - \nabla\cdot(\mathbf{k}\nabla\phi^h) + s\phi^h - f)d\Omega = \\
&=\int_\Omega w^h f d\Omega + \int_{\Gamma N} w^h g d\Gamma, \qquad \forall w^h \in V^h.
\end{aligned} \tag{A.6}$$

There are many forms of stabilization, being the SUPG one of them. Generally speaking, the Petrov-Galerkin formulation for the CDR equation is:

$$\begin{aligned}
&\int_\Omega \big(w^h(\mathbf{u}\cdot\nabla\phi^h) + \nabla w^h\cdot(\mathbf{k}\nabla\phi^h) + w^h s\phi^h\big)d\Omega + \\
&+\sum_{e=1}^{nel}\int_\Omega L_{St} w^h \tau(L_{CDR}\phi^h - f)d\Omega = \\
&=\int_\Omega w^h f d\Omega + \int_{\Gamma N} w^h g d\Gamma, \qquad \forall w^h \in V^h,
\end{aligned} \tag{A.7}$$

where L_{St} is the linear stabilization differential operator and L_{CDR} is the convection-diffusion-reaction differential operator. There are several stabilization operators, each one with its flaws and advantages. Stabilization operators used in this work are listed on table A.1.

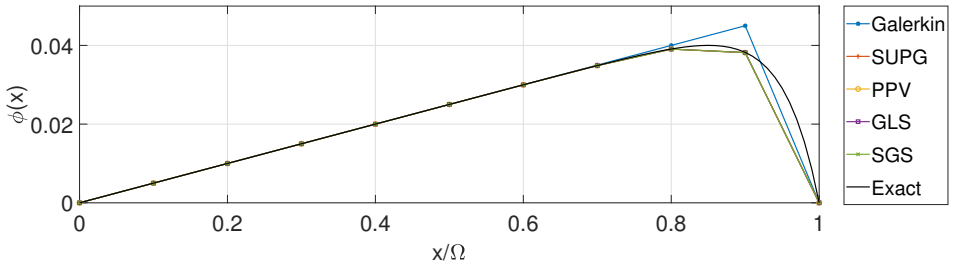

Figure A.3: Example with $Pe = 1$, $s = 0$, $f = 1$ and $\phi(0) = \phi(1) = 0$

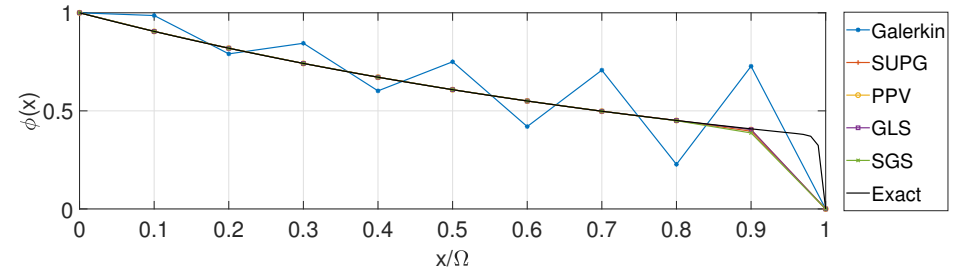

Figure A.4: Example with $Pe = 10$, $Da = 0.1$, $f = 0$ and $\phi(0) = 1$ and $\phi(1) = 0$

Table A.1: Differential operators on the weighting function for linear stabilization methods.

Method	Stabilization operator (L_{St})	Works
SUPG	$\mathbf{u} \cdot \nabla$	BROOKS and HUGHES [61]
GLS	$\mathbf{u} \cdot \nabla - \nabla \cdot (\mathbf{k}\nabla) + s$	HUGHES *et al.* [62]
SGS	$\mathbf{u} \cdot \nabla + \nabla \cdot (\mathbf{k}\nabla) - s$	HUGHES [63]
PPV	$\mathbf{u} \cdot \nabla - \nabla \cdot (\mathbf{k}\nabla) + \lvert s \rvert$	JOSHI and JAIMAN [60]

In one dimension, it can be assumed that $\mathbf{u} = u$ and $\mathbf{k} = k$. Some results are presented. A 10 linear element grid is used to show the versatility of the stabilization techniques. Figures A.3, A.4 and A.4 show how the Galerkin method presents unstable behaviour when the Peclét number becomes larger. When the Dahmköhler number is not significant, all the stabilization methods behave in a similar way. This is also confirmed after analyzing the methods in Table A.1. Since our simulations consist on linear finite elements, the stabilization terms related to diffusion are null. Thus, when the parameter s is not significant, all methods behave similarly to the SUPG method. This is the case for the examples described on Figs. A.3 and A.4. However, in situations where the reaction term is significant, the behaviour of the stabilization methods becomes different. Figure A.5 presents the results of a situation of this kind.

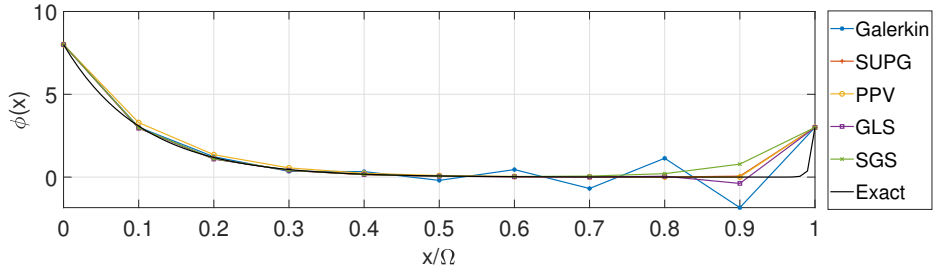

Figure A.5: Example with $Pe = 10$, $Da = 1$, $f = 0$ and $\phi(0) = 8$ and $\phi(1) = 3$